



**HAL**  
open science

# How partial melting affects small-scale convection in a plume-fed sublithospheric layer beneath fast-moving plates

Roberto Agrusta, Andrea Tommasi, Diane Arcay, Alicia Gonzalez, Taras Gerya

► **To cite this version:**

Roberto Agrusta, Andrea Tommasi, Diane Arcay, Alicia Gonzalez, Taras Gerya. How partial melting affects small-scale convection in a plume-fed sublithospheric layer beneath fast-moving plates. *Geochemistry, Geophysics, Geosystems*, 2015, 16 (11), pp.3924-3945. 10.1002/2015GC005967. hal-01277175

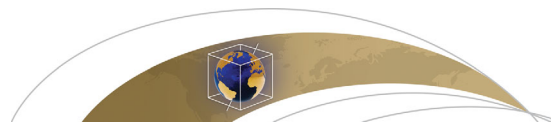
**HAL Id: hal-01277175**

**<https://hal.science/hal-01277175>**

Submitted on 19 Apr 2018

**HAL** is a multi-disciplinary open access archive for the deposit and dissemination of scientific research documents, whether they are published or not. The documents may come from teaching and research institutions in France or abroad, or from public or private research centers.

L'archive ouverte pluridisciplinaire **HAL**, est destinée au dépôt et à la diffusion de documents scientifiques de niveau recherche, publiés ou non, émanant des établissements d'enseignement et de recherche français ou étrangers, des laboratoires publics ou privés.



RESEARCH ARTICLE

10.1002/2015GC005967

Special Section:

The Lithosphere-Asthenosphere System

Key Points:

- Partial melting does not enhance basal erosion of the plate, but changes its location
- Buoyancy increase due to melt retention and depletion accelerates the onset, melt weakening not
- Latent heat of melting and accumulation of strongly depleted material delay the SSC onset

Supporting Information:

- Supporting Information S1

Correspondence to:

R. Agrusta,  
r.agrusta@imperial.ac.uk

Citation:

Agrusta, R., A. Tommasi, D. Arcay, A. Gonzalez, and T. Gerya (2015), How partial melting affects small-scale convection in a plume-fed sublithospheric layer beneath fast-moving plates, *Geochem. Geophys. Geosyst.*, 16, 3924–3945, doi:10.1002/2015GC005967.

Received 16 JUN 2015

Accepted 12 OCT 2015

Accepted article online 15 OCT 2015

Published online 14 NOV 2015

# How partial melting affects small-scale convection in a plume-fed sublithospheric layer beneath fast-moving plates

Roberto Agrusta<sup>1,2</sup>, Andrea Tommasi<sup>2</sup>, Diane Arcay<sup>2</sup>, Alicia Gonzalez<sup>2</sup>, and Taras Gerya<sup>3</sup>

<sup>1</sup>Department of Earth Science and Engineering, Imperial College London, London, UK, <sup>2</sup>Geosciences Montpellier, CNRS & Université de Montpellier, Montpellier, France, <sup>3</sup>Department of Geosciences, Swiss Federal Institute of Technology Zurich, Zürich, Switzerland

**Abstract** Numerical models show that small-scale convection (SSC) occurring atop a mantle plume is a plausible mechanism to rejuvenate the lithosphere. The triggering of SSC depends on the density contrast and on the rheology of the unstable layer underlying the stagnant upper part of the thermal boundary layer (TBL). Partial melting may change both properties. We analyze, using 2-D numerical simulations, how partial melting influences the dynamics of time-dependent SSC instabilities and the resulting thermo-mechanical rejuvenation of an oceanic plate moving atop of a plume. Our simulations show a complex behavior, with acceleration, no change, or delay of the SSC onset, due to competing effects of the latent heat of partial melting, which cools the plume material, and of the buoyancy increase associated with both melt retention and depletion of residue following melt extraction. The melt-induced viscosity reduction is too localized to affect significantly SSC dynamics. Faster SSC triggering is promoted for low melting degrees (low plume temperature anomalies, thick lithosphere, or fast moving plates), which limit both the temperature reduction due to latent heat of melting and the accumulation of depleted buoyant residue in the upper part of the unstable layer. In contrast, high partial melting degrees lead to a strong temperate decrease due to latent heat of melting and development of a thick depleted layer within the sublithospheric convecting layer, which delay the development of gravitational instabilities. Despite differences in SSC dynamics, the thinning of the lithosphere is not significantly enhanced relatively to simulations that neglect partial melting.

## 1. Introduction

Intraplate volcanic hotspots are proposed to be generated by plumes of hot material rising through the mantle [Morgan, 1972], consistently with the age progression of the volcanic chains, the geochemical signatures of lavas indicating partial melting of an enriched mantle, and the associated topographic swells [Morgan, 1972; Crough and Jurdy, 1980; Hart et al., 1992; Phipps Morgan et al., 1995]. A lithospheric plate passing atop such a plume is likely to be thermally thinned or “rejuvenated” [Sleep, 1994; Ribe, 2004]. Geophysical data on the lithosphere-asthenosphere boundary (LAB) depth beneath active hotspots corroborate this prediction, but the LAB upwelling inferred from various methods may differ significantly. Receiver function and surface wave data imaging the mantle beneath hotspots, such as Hawaii, Cape Verde and Galapagos, show a LAB up to 50 km shallower than the surroundings [Li et al., 2004; Lodge and Helffrich, 2006; Rychert et al.; 2013, 2014; Villagomez et al., 2014; Byrnes et al., 2015]. Underside reflection data suggest that the Pacific lithosphere is thinned by ~10 km along the Hawaiian chain over a lateral scale of ~1000 km [Schmerr, 2012]. A gravimetric study in Hawaii shows that the geoid-to-topography ratio varies along the swell, indicating a decrease of the average depth of compensation by 20 km [Cadio et al., 2012].

Numerical models show that development of small-scale convection (SSC) in the low viscosity layer formed by the spreading of the hot plume material along the base of the moving lithospheric plate may promote bottom-up erosion of the lithosphere by up to 30 km [Moore et al., 1998; Thoraval et al., 2006; Agrusta et al., 2013]. However, these studies do not consider the influence of partial melting on the dynamics of the plume-lithosphere interactions. Partial melting may have multiple consequences on SSC dynamics. The absorption/release of latent heat during melting/crystallization may affect the thermal structure, and, consequently, the thermal buoyancy [McKenzie and Bickle, 1988]. Effective buoyancy may also increase as a consequence of (1) melt retention [Scott and Stevenson, 1989] and (2) removal of dense elements from the solid

residue [Oxburgh and Parmentier, 1977; Jordan, 1979; Schutt and Leshner, 2006]. Moreover, convection may be enhanced as a result of lower viscosities in partially molten domains in the mantle, since the presence of melt fractions as low as 1% may decrease the peridotite strength by more than one order of magnitude [Faul and Jackson, 2007; Takei and Holtzman, 2009a].

To our knowledge, the dynamic effects of partial melting on the plume-fed sublithospheric layer behavior and on the resulting uplift of the LAB have not been considered before. Previous models that simulated partial melting associated with a mantle plume impact focused on the melt-production rate, trying to constrain, on one hand, the total melt production and the composition of primary magma sources and, on the other hand, the influence of lithosphere extension on melt generation. These works showed that during the first phases of mantle plume activity, 90% of the magma originates from partial melting of the plume head [e.g., Watson and McKenzie, 1990; Farnetani and Richards, 1994, 1995]. Other models analyzed the causes of spatial and temporal variations of the melting rate within the plume material as it spreads along the base of the lithosphere [Ribe and Christensen, 1999; Bianco et al., 2008, 2011; Ballmer et al., 2011]. They showed that partial melting may occur both in a primary partial melting zone located above the plume stem and in smaller secondary partial melting zones located downstream from the first due to further decompression associated with the development of small-scale convection in the plume-fed layer. Predicted magma compositions evolve in time and space: the early stages of volcanism display a strong signature from a deep partial melting component, whereas the late magmatism records shallow melting [Bianco et al., 2008, 2011]. In addition, Ballmer et al. [2011] showed that the topography of the base of the lithosphere resulting from SSC controls the spreading of the hot plume material, generating an asymmetry of the partial melting structure that could explain the differences in lavas geochemistry between the Southern (Loa) and Northern (Kea) trends of Hawaiian volcanoes [Abouchami et al., 2005].

The effect of partial melting on the mechanical structure of the lithosphere has been investigated only in the particular case of a plume head impacting a stationary plate [Manglik and Christensen, 1997]. This study showed that the increased buoyancy of the depleted residue formed by melt extraction after decompression melting in the plume initially accelerates the development of small-scale instabilities at the bottom of the lithosphere. However, evolution of this process results in a thick depleted root beneath the lithosphere, which inhibits further thermo-mechanical erosion of the plate.

In this paper, we investigate the influence of both viscosity and density variations arising from partial melting on the SSC dynamics in the sublithospheric plume-fed layer and on the resulting lithospheric erosion in models where a mantle plume interacts with a fast-moving plate.

## 2. Model Setup

### 2.1. Numerical Code and Boundary Conditions

The influence of partial melting on plume-lithosphere interactions is simulated using the 2-D thermo-mechanical code I2VIS [Gerya and Yuen, 2003]. We solve on a staggered grid the equations of conservation of mass, momentum, and energy for an incompressible, infinite Prandtl number fluid. The advection term in the heat equation is handled by the marker-in-cell method. We include the adiabatic heating, viscous dissipation, and latent heat of melting/crystallization terms in the energy equation (extended Boussinesq approximation [Christensen and Yuen, 1985]). Radiogenic heat production is neglected. The adiabatic ( $H_a$ ) and viscous ( $H_s$ ) heating production terms are:

$$H_a = T\alpha\rho v_y g, \quad \text{and} \quad H_s = \sigma_{xx}\epsilon_{xx} + \sigma_{yy}\epsilon_{yy} + 2\sigma_{xy}\epsilon_{xy}, \quad (1)$$

where  $x$  and  $y$  denote the horizontal and vertical coordinates, respectively,  $v_y$  is the vertical velocity component,  $T$  is temperature,  $\rho$  is density,  $\alpha$  is the thermal expansion coefficient,  $g$  is the acceleration due to gravity,  $\sigma_{ij}$  are the components of the deviatoric stress tensor, and  $\epsilon_{ij}$  are the components of the deviatoric strain-rate tensor. The latent heat of melting/crystallization is simulated by adjusting the effective heat capacity,  $C_{Peff}$ , and thermal expansion,  $\alpha_{eff}$ , of the partially molten/crystallized rocks [Schubert et al., 1975; Christensen and Yuen, 1985; Stüwe, 1995] at each time step, as:

**Table 1.** Physical Parameters

| Symbol                              | Meaning                 | Value  | Unit   |
|-------------------------------------|-------------------------|--|--|
| <i>General Parameters</i>           |                         |  |  |
| $H$                                 | Box height              | 700  | km   |
| $L$                                 | Box width               | 4000   | km   |
| $T_0$                               | Surface temperature     | 273  | K  |
| $T_1$                               | Bottom temperature      | 1837   | K  |
| $g$                                 | Gravity                 | 10   | $\text{m}\cdot\text{s}^{-2}$                     |
| $k$                                 | Thermal conductivity    | 3.2  | $\text{W}\cdot\text{m}^{-1}\cdot\text{K}^{-1}$   |
| $C_p$                               | Heat capacity           | 1250   | $\text{J}\cdot\text{kg}^{-1}\cdot\text{K}^{-1}$  |
| $R$                                 | Gas constant            | 8.314  | $\text{J}\cdot\text{K}^{-1}\cdot\text{mol}^{-1}$ |
| <i>Rheological Model Parameters</i> |                         |  |  |
| $\mu_0$                             | Preexponential          | $3.9 \times 10^{10}$<br>$5.3 \times 10^{10}$ | Pa·s   |
| $E_a$                               | Activation energy       | $2.5 \times 10^5$                            | $\text{J}\cdot\text{mol}^{-1}$                   |
| $V_a$                               | Activation Volume       | $4.8 \times 10^{-6}$                         | $\text{m}^3\cdot\text{mol}^{-1}$                 |
| $A$                                 | Contiguity prefactor    | 2.3  |  |
| <i>Density Model Parameters</i>     |                         |  |  |
| $\rho_{sr}$                         | Reference solid density | 3300   | $\text{kg}\cdot\text{m}^{-3}$                    |
| $\alpha_s$                          | Solid thermal expansion | $3 \times 10^{-5}$                           | $\text{K}^{-1}$                                  |
| $\beta_s$                           | Solid compressibility   | $7.8 \times 10^{-3}$                         | $\text{GPa}^{-1}$                                |
| $\rho_{lr}$                         | Reference melt density  | 2700   | $\text{kg}\cdot\text{m}^{-3}$                    |
| $\alpha_l$                          | Melt thermal expansion  | $5 \times 10^{-5}$                           | $\text{K}^{-1}$                                  |
| $\beta_l$                           | Melt compressibility    | $40 \times 10^{-3}$                          | $\text{GPa}^{-1}$                                |
| <i>Melting Model Parameters</i>     |                         |  |  |
| $Q_L$                               | Latent heat             | 300  | $\text{kJ}\cdot\text{kg}^{-1}$                   |

$$C_{peff} = C_p + Q_L \left( \frac{\partial M}{\partial T} \right)_P, \text{ and} \quad (2)$$

$$\alpha_{eff} = \alpha + \rho \frac{Q_L}{T} \left( \frac{\partial M}{\partial P} \right)_T,$$

where  $Q_L$  is the latent heat of melting/crystallization for a peridotite,  $M$  the weight fraction of melt (see section 2.2), and  $P$  is the pressure.  $C_p$  and  $\alpha$  in equation (2) refer to heat capacity and thermal expansion of the solid peridotite. Table 1 lists all model parameters.

The model domain is 4000 km wide and 700 km high and has an initially homogeneous fertile peridotite composition (Figure 1). The box is discretized into  $427 \times 96$  nodes. The mesh is refined vertically between 0 and 250 km depth and horizontally between  $-130$  km and 130 km from the center of the box, where the  $x$ - and  $y$ -spacing is set to 5 km. The  $x$ - and  $y$ -spacing is 10 km outside the refined

domains. The refined areas correspond to the lithosphere and the sublithospheric layer, where plume-lithosphere interactions take place, and to the area where the plume rises. The box is initially filled by 1,942,560 particles with a uniform density corresponding to a minimum of 16 markers in the smallest mesh. The numerical resolution in mesh size and marker density was validated in a previous study [Agrusta et al., 2013].

Mechanical boundary conditions are depicted in Figure 1a. The bottom and right boundaries are open. External no slip conditions are nevertheless imposed on these boundaries. This results in a constant velocity gradient along the boundary:

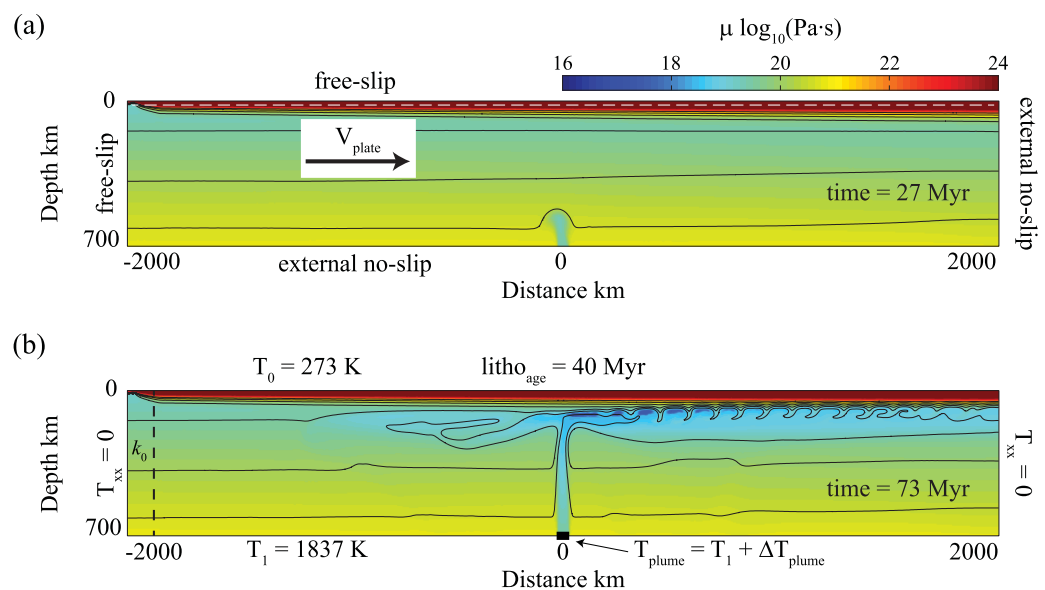


**Figure 1.** Snapshots of the model set-up for simulation 6 (Table 2) at (a) 27 Myr and (b) 73 Myr after the introduction of the thermal anomaly. The color scale represents the viscosity field and the contour lines the isotherms from 1200 to 1800°C spaced by 100°C. (a) Mechanical boundary conditions. (b) Thermal boundary conditions including those generating and sustaining plume upwelling.

$$\frac{\delta v_i}{\delta x_i} \Delta L + v_i = 0, \quad (3)$$

where  $\Delta L$  is the distance away from the actual boundary where the no slip condition ( $v_i = 0$ ) is satisfied [for details, see *Agrusta et al.*, 2013]. This distance controls the velocity gradient at the boundary. A real natural open boundary, simulated by a constant flux, is reproduced if  $\Delta L$  is infinite. In the present simulations, to ensure numerical stability, a seminatural open boundary is modeled by imposing very low velocity gradients normal to the bottom and right-lateral open boundaries, for which  $\Delta L$  is set to 7368 and 9389 km, respectively.

Constant temperatures,  $T_o$  of 273 K and  $T_i$  of 1837 K, are imposed at the top and bottom of the box, respectively. Lateral boundaries are insulating. The initial temperature field, representing an oceanic plate cooling from a ridge located at the top left corner of the model ( $x = -2000$  km), is obtained by running preliminary simulations until thermal equilibrium is achieved for each imposed plate velocity (usually after 100 Myr). In most simulations, the cooling lithosphere is 40 Myr-old when it reaches the middle of the box ( $x = 0$  km), where it will be impinged by the ascending plume, for all plate velocities, since we increase the thermal conductivity for the entire depth of the first 150 km of the model (measured laterally from the ridge location) to accelerate artificially the lithosphere cooling and limit the box size [*Agrusta et al.*, 2013]. In this domain, the increased thermal conductivity,  $k_o$ , is:

$$k_o = k \left( \text{age} - \frac{X_1}{V_{plate}} \right) \frac{V_{plate}}{X_o}, \quad (4)$$

where  $k$  is the reference thermal conductivity of the upper mantle (Table 1),  $\text{age}$  is 40 Myr,  $X_o$  is 150 km,  $X_1$  is 1850 km, and  $V_{plate}$  is the plate velocity. The plume is generated by modifying locally the bottom boundary condition: a temperature anomaly, defined as  $T_{plume} = T_i + \Delta T_{plume}$ , is constantly imposed on a 50 km wide domain centered at  $x = 0$  km at the bottom of the box (Figure 1b). To assess the effect of the thermal structure of the lithosphere on the plume-lithosphere interaction, we also run simulations in which the lithosphere is either 20 Myr or 80 Myr old at the plume impact point.

## 2.2. Partial Melting Model

To predict the onset of partial melting, we use a parameterization for batch melting under anhydrous conditions [*Katz et al.*, 2003]. The melting degree is calculated at each time iteration for all particles located at depths shallower than 250 km (0–8 GPa, corresponding to the pressure range for which the *Katz et al.* [2003] parameterization has been established). This depth limit is not a shortcoming, as partial melting never occurs deeper than 150 km in any of our simulations.

At the initiation of partial melting, the weight fraction of melt,  $M$ , is a function of temperature and pressure according to the relationship:

$$M = \frac{T - T(P)_{solidus}}{T(P)_{liquidus} - T(P)_{solidus}}, \quad (5)$$

with  $M = 0$  if  $T < T_{solidus}$  and  $M = 1$  if  $T > T_{liquidus}$ .  $T_{solidus} = 1085.7 + 132.9 \cdot P - 5.1 \cdot P^2$  and  $T_{liquidus} = 1780 + 45 \cdot P - 2 \cdot P^2$  are defined in °C with  $P$  being the pressure in GPa.

Progressive depletion of the solid residue, as fertile components segregate in the expelled magma, results in an increase of the peridotite solidus temperature [*Walter*, 1998]. The consequent decrease in melt production is modeled by considering the effective instantaneous melt production,  $\Delta M$ , as the difference between the partial melting degree predicted by equation (5) and the cumulated melt amount produced by the particle, set equal to the depletion degree (see equation (6) below). Since the melting degree of a rock particle is assumed to only strictly increase through time, if the predicted instantaneous melting degree is lower than, or equal to the cumulated one, the simulated instantaneous melt production is zero.

The depletion degree,  $F$ , is the cumulative sum through time of the melt fraction produced at each time step,  $\Delta M$ .  $F$  is defined at a given time step,  $n_t$ , as:

$$\text{if } M^{n_t} > F^{n_t-1}, F^{n_t} = F^{n_t-1} + \Delta M, \text{ with } \Delta M = M^{n_t} - F^{n_t-1} \quad (6)$$

Note that we do not model partial melting below the simulated pseudo-ridge located in the top left corner of the box, that is, in the first 500 km measured from the ridge axis. Partial melting and melt extraction at

the ridge should result in depletion of the first ~50 km of the lithosphere. In the present models, we neglect this ridge-related depletion because the shallow lithosphere only plays a role in plume-plate interactions when the plume impacts very young plates (<20 Myr old).

The melt weight fraction,  $M$ , is related to the volume fraction of melt ( $\phi$ ) through

$$\frac{1}{\phi} = 1 - \frac{\rho_{lr}}{\rho_{sr}} + \frac{1}{M} \frac{\rho_{lr}}{\rho_{sr}}, \quad (7)$$

where  $\rho_{lr}$  and  $\rho_{sr}$  are the densities of the melt and solid peridotite at the reference temperature,  $T_r = 298.15$  K, and pressure,  $P_r = 0.1$  MPa (Table 1).

In a batch melting model, the liquid is supposed to remain in chemical equilibrium with the solid residue; this model assumes no relative movement between the melt and the solid matrix. This conjecture is probably unrealistic when the melt fraction exceeds 1–2% [McKenzie, 1985a]. We parameterize melt extraction using a dynamic partial melting approximation, i.e., the melt is retained in the solid matrix until melt fraction reaches the critical threshold  $\phi_c$  at which previously isolated melt pockets form an interconnected network and become mobile. The porosity threshold in the upper mantle is not accurately known and is estimated to range from ~0.1 to 2% [McKenzie, 1985b, 2000; Riley and Kohlstedt, 1991; Faul, 2001]. Any melt fraction exceeding  $\phi_c$  is instantaneously extracted from the simulation box, assuming that the time scales of melt extraction and migration through the overlying column of mantle are much faster than that of mantle flow. Once melting stops at time step  $n_t$  (with  $\Delta M^{n_t-1} \neq 0$ ), we mimic the crystallization of the retained melt fraction  $\phi_c$  and the associated refertilization of the residual peridotite by decreasing the depletion degree  $F$  by  $\phi_c$  if  $\Delta M^{n_t-1} \geq \phi_c$ , or by  $\Delta M^{n_t-1}$  if  $\Delta M^{n_t-1} < \phi_c$ .

### 2.3. Rheology

The viscosity of the unmolten peridotite ( $\mu_{cc}$ ) is modeled as:

$$\mu_{cc} = \mu_0 \exp\left(\frac{E_a + V_a P}{RT}\right), \quad (8)$$

where  $\mu_0$  is preexponential factor,  $E_a$  is the activation energy,  $V_a$  is the activation volume, and  $R$  is the gas constant (Table 1). The viscosity of the partially molten peridotite is computed using a constitutive relationship based on a contiguity model, which considers the effects of melt distribution at the grain-scale as observed in laboratory experiments [Takei and Holtzman, 2009a]. In this model, the macroscopic viscosity depends not only on the volume melt fraction,  $\phi$ , but also on the distribution of liquid pockets at the grain scale. The macroscopic relationship between stress and strain rate depends therefore on the crystal contiguity,  $\varphi$ , defined as:

$$\varphi = 1 - A\phi^{0.3}, \quad (9a)$$

where  $A$  is a parameter depending on composition, which here equals 2.3. This model predicts a drastic reduction (by a factor 5) in the aggregate viscosity,  $\mu$ , associated with a change from diffusion through grain boundaries to diffusion through the liquid, occurring at a critical melt fraction, which depends on grain size. For a grain size of 3 mm, which is consistent with observations of mantle samples deformed near solidus conditions [e.g., Le Roux et al., 2008; Higgie and Tommasi, 2012, 2014], the critical melt fraction is estimated to be 0.01 wt % [Takei and Holtzman, 2009b]. In this framework, in a partially molten peridotite, the total deformation is the sum of grain deformation by diffusion, grain boundary sliding, reactions at the solid-liquid phase boundary, and matter diffusion through the liquid phase. The resulting constitutive relationship, if  $0.01\% \leq \phi \leq \phi_c$  is:

$$\mu = 0.2\mu_{cc}\varphi^2. \quad (9b)$$

In the present models a lower and an upper viscosity cutoffs are imposed at  $10^{16}$  Pa·s and  $10^{24}$  Pa·s, respectively.

By assuming the mantle to be made of anhydrous peridotite, we neglect the influence of dehydration due to partial melting on the peridotite rheology. This choice is justified by the uncertainty concerning the actual effect of hydration on olivine rheology: experimental estimates of hydrolytic weakening in olivine

range from four orders of magnitude [Karato, 2010] to a factor 2–3 [Demouchy et al., 2012; Girard et al., 2013; Fei et al., 2013].

#### 2.4. Density

Density depends on temperature,  $T$ , pressure,  $P$ , volume fraction of melt,  $\phi$ , and depletion degree,  $F$ :

$$\rho = (1 - \phi)\rho_s + \phi\rho_l, \quad (10)$$

with

$$\begin{aligned} \rho_l &= \rho_{lr} [1 - \alpha_l(T - T_r)] [1 + \beta_l(P - P_r)] \\ \rho_s &= [(1 - F)\rho_{sr} + F\rho_{dep}] [1 - \alpha_s(T - T_r)] [1 + \beta_s(P - P_r)], \end{aligned} \quad (11)$$

where  $\rho_s$  and  $\rho_l$  are the densities calculated using the reference densities  $\rho_{sr}$  and  $\rho_{lr}$  at ambient conditions,  $\alpha_s$  and  $\alpha_l$  are the thermal expansion coefficients, and  $\beta_s$  and  $\beta_l$  are the compressibilities for the solid and the melt, respectively (Table 1). The variation in solid density due to depletion,  $\rho_{dep}$ , is calculated using a parameterized relationship of the residuum density of lherzolite melting, which is valid for 0 to 35% of melt extraction in the 0–7 GPa pressure range [Schutt and Leshner, 2006]. This relation predicts a density reduction of 1–2% for 20% of melt extraction.

$$\frac{\rho_{dep}}{\rho_{sr}} = \alpha_0 + \alpha_1 P + \alpha_2 P^2 + \alpha_3 P^3 + \alpha_4 P^4 + \alpha_5 F + \alpha_6 FP, \quad (12)$$

where  $P$  is in GPa, and  $\alpha_0 = 0.972$ ,  $\alpha_1 = 4.79 \times 10^2 \text{ GPa}^{-1}$ ,  $\alpha_2 = -2.21 \times 10^2 \text{ GPa}^{-2}$ ,  $\alpha_3 = 3.81 \times 10^3 \text{ GPa}^{-3}$ ,  $\alpha_4 = -2.21 \times 10^4 \text{ GPa}^{-4}$ ,  $\alpha_5 = -2.80 \times 10^4$ ,  $\alpha_6 = -2.53 \times 10^5 \text{ GPa}^{-1}$ .

### 3. Model Results

A total of 96 simulations (Table 2) have been performed considering three plate velocities,  $V_{plate}$ : 7.5, 10, and 12.5  $\text{cm}\cdot\text{yr}^{-1}$ , and two different background mantle viscosities,  $\mu_1$ , defined at the bottom of the box ( $H = 700 \text{ km}$  and  $T_1 = 1837 \text{ K}$ ):  $7.5 \times 10^{20}$  and  $10^{21} \text{ Pa}\cdot\text{s}$ . The imposed plume thermal anomaly,  $\Delta T_{plume}$ , ranges from 250 to 375 K. As the plume upwelling velocity depends on both the thermal anomaly and the background mantle viscosity, we characterize the plume vigor by the plume Rayleigh number  $Ra_{plume} = (\alpha g \rho_{sr} H^3 (T_{plume} - T_0)) / (\kappa \mu_{plume})$ , where  $\mu_{plume}$  is the viscosity at the temperature  $T_{plume}$  at the bottom of the box.

For each  $V_{plate}$ ,  $\mu_1$ , and  $\Delta T_{plume}$  set, two simulations are performed: one neglecting the effects of partial melting on viscosity, density, and on the temperature field (latent heat), hereafter referred to as melt-free cases, and one considering all these effects (equations (2), (9), and (10)), hereafter referred to as melt-dependent cases, using a volume threshold for the melt extraction,  $\phi_C$ , of 1%.

Additional simulations have been performed neglecting the latent heat of melting (equation (2)), but considering the effects of partial melting on viscosity and density. The influence of plate age at the impact point is tested by running 12 additional experiments in which the age of the lithosphere at the plume impact point is either 20 Myr or 80 Myr. The influence of the liquid extraction threshold,  $\phi_C$ , is tested by varying it from 0.5 to 5% in simulation 16 (simulations 16c2 to 16f3). For this particular case, the respective contributions of viscosity and density dependence in melting degree were also investigated separately.

In all simulations, the plume rises through the mantle and spreads out along the base of the lithosphere asymmetrically, as illustrated in Figure 2. The vigor of the downstream flow (in the plate motion direction) with respect to upstream flow depends on the ratio of the plume upwelling velocity to the plate speed. High plate velocities and slow plume upwellings favor downstream flow of the plume material [Agrusta et al., 2013]. Cold dripping instabilities initiate within the sublayer located at the transition between the lithosphere and the plume-fed asthenosphere. As they grow, these instabilities are advected by the downstream flow away from the plume conduit. A few instabilities also develop upstream of the plume stem, in particular for vigorous plumes and/or slow plate velocities.

Figure 2 (top) shows the vertically integrated (over the whole box) instantaneous and accumulated mass of melt (in  $\text{kg}\cdot\text{m}^{-2}$ ) as a function of the distance from the plume impact. Figure 2 (bottom) displays the

**Table 2.** Simulations List<sup>a</sup>

| Run   | $\mu_{mantle}$<br>(Pa·s) | $V_{plate}$<br>(cm·yr <sup>-1</sup> ) | $\Delta T_{plume}$<br>(K) | $Ra_{plume}$<br>( $\times 10^7$ ) | Plate age<br>Myr | $Q_L$ | $\phi_C$ (%) | Melt-Dependent<br>Properties | $\tau_C \times 10^{-4}$ |          |            |
|-------|--------------------------|---------------------------------------|---------------------------|-----------------------------------|------------------|-------|--------------|------------------------------|-------------------------|----------|------------|
|       |                          |                                       |                           |                                   |                  |       |              |                              | Melt-Free               | Melt-Dep | SSC Change |
| 1     | $7.5 \times 10^{20}$     | 7.5                                   | 250                       | 2.11 (1)                          | 40               | Y     | 1            | $\mu(\phi) - \rho(\phi, F)$  | 3.16                    | 3.29     | 0          |
| 2     | $7.5 \times 10^{20}$     | 7.5                                   | 275                       | 2.73 (3)                          | 40               | Y     | 1            | $\mu(\phi) - \rho(\phi, F)$  | 2.68                    | 2.83     | 0          |
| 3     | $7.5 \times 10^{20}$     | 7.5                                   | 300                       | 3.51 (5)                          | 40               | Y     | 1            | $\mu(\phi) - \rho(\phi, F)$  | 2.44                    | 2.99     | -1         |
| 4     | $7.5 \times 10^{20}$     | 7.5                                   | 325                       | 4.49 (7)                          | 40               | Y     | 1            | $\mu(\phi) - \rho(\phi, F)$  | 2.26                    | 2.71     | -1         |
| 5     | $7.5 \times 10^{20}$     | 10                                    | 250                       | 2.11 (1)                          | 40               | Y     | 1            | $\mu(\phi) - \rho(\phi, F)$  | 3.25                    | 2.92     | 1          |
| 6     | $7.5 \times 10^{20}$     | 10                                    | 275                       | 2.73 (3)                          | 40               | Y     | 1            | $\mu(\phi) - \rho(\phi, F)$  | 2.45                    | 1.86     | 1          |
| 6b    | $7.5 \times 10^{20}$     | 10                                    | 275                       | 2.73 (3)                          | 40               | N     | 1            | $\mu(\phi) - \rho(\phi, F)$  | 2.45                    | 1.56     | 1          |
| 7     | $7.5 \times 10^{20}$     | 10                                    | 300                       | 3.51 (5)                          | 40               | Y     | 1            | $\mu(\phi) - \rho(\phi, F)$  | 2.02                    | 2.09     | 0          |
| 7b    | $7.5 \times 10^{20}$     | 10                                    | 300                       | 3.51 (5)                          | 40               | N     | 1            | $\mu(\phi) - \rho(\phi, F)$  | 2.02                    | 1.85     | 1          |
| 8     | $7.5 \times 10^{20}$     | 10                                    | 325                       | 4.49 (7)                          | 40               | Y     | 1            | $\mu(\phi) - \rho(\phi, F)$  | 1.83                    | 1.75     | 0          |
| 8b    | $7.5 \times 10^{20}$     | 10                                    | 325                       | 4.49 (7)                          | 40               | N     | 1            | $\mu(\phi) - \rho(\phi, F)$  | 1.83                    | 1.45     | 1          |
| 9     | $7.5 \times 10^{20}$     | 12.5                                  | 300                       | 3.51 (5)                          | 40               | Y     | 1            | $\mu(\phi) - \rho(\phi, F)$  | 2.23                    | 1.28     | 1          |
| 10    | $7.5 \times 10^{20}$     | 12.5                                  | 325                       | 4.49 (7)                          | 40               | Y     | 1            | $\mu(\phi) - \rho(\phi, F)$  | 1.58                    | 1.86     | 0          |
| 11    | $7.5 \times 10^{20}$     | 12.5                                  | 350                       | 5.72 (9)                          | 40               | Y     | 1            | $\mu(\phi) - \rho(\phi, F)$  | 1.43                    | 1.33     | 0          |
| 12    | $10^{21}$                | 7.5                                   | 300                       | 2.63 (2)                          | 40               | Y     | 1            | $\mu(\phi) - \rho(\phi, F)$  | 2.82                    | 3.11     | 0          |
| 12b   | $10^{21}$                | 7.5                                   | 300                       | 2.63 (2)                          | 40               | N     | 1            | $\mu(\phi) - \rho(\phi, F)$  | 2.82                    | 2.89     | 0          |
| 13    | $10^{21}$                | 7.5                                   | 325                       | 3.37 (4)                          | 40               | Y     | 1            | $\mu(\phi) - \rho(\phi, F)$  | 2.53                    | 3.07     | -1         |
| 14    | $10^{21}$                | 7.5                                   | 350                       | 4.29 (6)                          | 40               | Y     | 1            | $\mu(\phi) - \rho(\phi, F)$  | 2.33                    | 2.87     | -1         |
| 14b   | $10^{21}$                | 7.5                                   | 350                       | 4.29 (6)                          | 40               | N     | 1            | $\mu(\phi) - \rho(\phi, F)$  | 2.33                    | 2.06     | 1          |
| 15    | $10^{21}$                | 7.5                                   | 375                       | 5.43 (8)                          | 40               | Y     | 1            | $\mu(\phi) - \rho(\phi, F)$  | 2.12                    | 2.88     | -1         |
| 16    | $10^{21}$                | 10                                    | 300                       | 2.63 (2)                          | 40               | Y     | 1            | $\mu(\phi) - \rho(\phi, F)$  | 3.08                    | 1.63     | 1          |
| 16c2  | $10^{21}$                | 10                                    | 300                       | 2.63 (2)                          | 40               | Y     | 1            | $\rho(\phi, F)$              | 3.08                    | 1.67     | 1          |
| 16c3  | $10^{21}$                | 10                                    | 300                       | 2.63 (2)                          | 40               | Y     | 1            | $\mu(\phi)$                  | 3.08                    | 3.23     | 0          |
| 16b   | $10^{21}$                | 10                                    | 300                       | 2.63 (2)                          | 40               | N     | 1            | $\mu(\phi) - \rho(\phi, F)$  | 3.08                    | 1.57     | 1          |
| 16d1  | $10^{21}$                | 10                                    | 300                       | 2.63 (2)                          | 40               | Y     | 0.5          | $\mu(\phi) - \rho(\phi, F)$  | 3.08                    | 2.02     | 1          |
| 16d2  | $10^{21}$                | 10                                    | 300                       | 2.63 (2)                          | 40               | Y     | 0.5          | $\rho(\phi, F)$              | 3.08                    | 1.97     | 1          |
| 16d3  | $10^{21}$                | 10                                    | 300                       | 2.63 (2)                          | 40               | Y     | 0.5          | $\mu(\phi)$                  | 3.08                    | 3.22     | 0          |
| 16e1  | $10^{21}$                | 10                                    | 300                       | 2.63 (2)                          | 40               | Y     | 2            | $\mu(\phi) - \rho(\phi, F)$  | 3.08                    | 1.3      | 1          |
| 16e2  | $10^{21}$                | 10                                    | 300                       | 2.63 (2)                          | 40               | Y     | 2            | $\rho(\phi, F)$              | 3.08                    | 1.45     | 1          |
| 16e3  | $10^{21}$                | 10                                    | 300                       | 2.63 (2)                          | 40               | Y     | 2            | $\mu(\phi)$                  | 3.08                    | 3.21     | 0          |
| 16f1  | $10^{21}$                | 10                                    | 300                       | 2.63 (2)                          | 40               | Y     | 5            | $\mu(\phi) - \rho(\phi, F)$  | 3.08                    | 1.16     | 1          |
| 16f2  | $10^{21}$                | 10                                    | 300                       | 2.63 (2)                          | 40               | Y     | 5            | $\rho(\phi, F)$              | 3.08                    | 1.32     | 1          |
| 16f3  | $10^{21}$                | 10                                    | 300                       | 2.63 (2)                          | 40               | Y     | 5            | $\mu(\phi)$                  | 3.08                    | 3.05     | 0          |
| 16a20 | $10^{21}$                | 10                                    | 300                       | 2.63 (2)                          | 20               | Y     | 1            | $\mu(\phi) - \rho(\phi, F)$  | 2.63                    | 3.02     | 0          |
| 17    | $10^{21}$                | 10                                    | 325                       | 3.37 (4)                          | 40               | Y     | 1            | $\mu(\phi) - \rho(\phi, F)$  | 2.14                    | 2.13     | 0          |
| 17b   | $10^{21}$                | 10                                    | 325                       | 3.37 (4)                          | 40               | N     | 1            | $\mu(\phi) - \rho(\phi, F)$  | 2.14                    | 1.95     | 1          |
| 17a20 | $10^{21}$                | 10                                    | 325                       | 3.37 (4)                          | 20               | Y     | 1            | $\mu(\phi) - \rho(\phi, F)$  | 1.96                    | 2.07     | 0          |
| 17a80 | $10^{21}$                | 10                                    | 325                       | 3.37 (4)                          | 80               | Y     | 1            | $\mu(\phi) - \rho(\phi, F)$  | 2.87                    | 1.8      | 1          |
| 18    | $10^{21}$                | 10                                    | 350                       | 4.29 (6)                          | 40               | Y     | 1            | $\mu(\phi) - \rho(\phi, F)$  | 1.97                    | 1.85     | 0          |
| 18b   | $10^{21}$                | 10                                    | 350                       | 4.29 (6)                          | 40               | N     | 1            | $\mu(\phi) - \rho(\phi, F)$  | 1.97                    | 1.26     | 1          |
| 19    | $10^{21}$                | 10                                    | 375                       | 5.43 (8)                          | 40               | Y     | 1            | $\mu(\phi) - \rho(\phi, F)$  | 1.76                    | 1.74     | 0          |
| 20    | $10^{21}$                | 12.5                                  | 300                       | 2.63 (2)                          | 40               | Y     | 1            | $\mu(\phi) - \rho(\phi, F)$  | 2.88                    | 1.72     | 1          |
| 20a20 | $10^{21}$                | 12.5                                  | 300                       | 2.63 (2)                          | 20               | Y     | 1            | $\mu(\phi) - \rho(\phi, F)$  | 2.81                    | 1.26     | 1          |
| 21    | $10^{21}$                | 12.5                                  | 325                       | 3.37 (4)                          | 40               | Y     | 1            | $\mu(\phi) - \rho(\phi, F)$  | 2.44                    | 1.36     | 1          |
| 22    | $10^{21}$                | 12.5                                  | 350                       | 4.29 (6)                          | 40               | Y     | 1            | $\mu(\phi) - \rho(\phi, F)$  | 1.74                    | 1.93     | 0          |
| 22a20 | $10^{21}$                | 12.5                                  | 350                       | 4.29 (6)                          | 20               | Y     | 1            | $\mu(\phi) - \rho(\phi, F)$  | 1.61                    | 1.07     | 0          |
| 22a80 | $10^{21}$                | 12.5                                  | 350                       | 4.29 (6)                          | 80               | Y     | 1            | $\mu(\phi) - \rho(\phi, F)$  | 2.02                    | 1.38     | 1          |
| 23    | $10^{21}$                | 12.5                                  | 375                       | 5.43 (8)                          | 40               | Y     | 1            | $\mu(\phi) - \rho(\phi, F)$  | 1.52                    | 1.21     | 0          |

<sup>a</sup>The number in the parenthesis in the column  $Ra_{plume}$  indicates the vigor of the plume (1 = weak plumes, 9 = strong plumes). The column  $Q_L$  indicates if latent heat effects (equation (2)) are considered (y) or not (n). The column  $\phi_C$  indicates the melt extraction threshold used for the different cases of simulation 16. The column  $\tau_C$  is the SSC onset time (dimensionless). The column SSC change expresses the change in the onset time of the SSC in melt-dependent ('Melt-Dep') relative to the equivalent 'Melt-Free' simulations (-1 = SSC-delayed; 0 = SSC-unchanged; 1 = SSC-acceleration).

temperature field, the partial melting regions, and the depletion degree across the model. Partial melting initiates at the plume head impact at the base of the lithosphere. In this area is produced the highest amount of melt ( $1.37 \text{ kg}\cdot\text{m}^{-2}$ ) (Figure 2a). It results from the continuous feeding of fertile and hot material by the upwelling plume. As the plume spreads out, partial melting stops due to depletion, and the depleted material is advected away from the plume axis. Secondary partial melting, producing lower melt volumes, is triggered away from the plume impact point by further decompression in the upwelling domains of the SSC. This secondary partial melting therefore occurs in small isolated domains with a wavelength of  $\sim 100 \text{ km}$ , that is, the SSC cell wavelength, up to  $\sim 1500 \text{ km}$  away from the plume impact (Figures 2b and 2c). It yields an increase of the depletion degree in the sublithospheric layer, which at some point (close to 20 wt %) hinders any

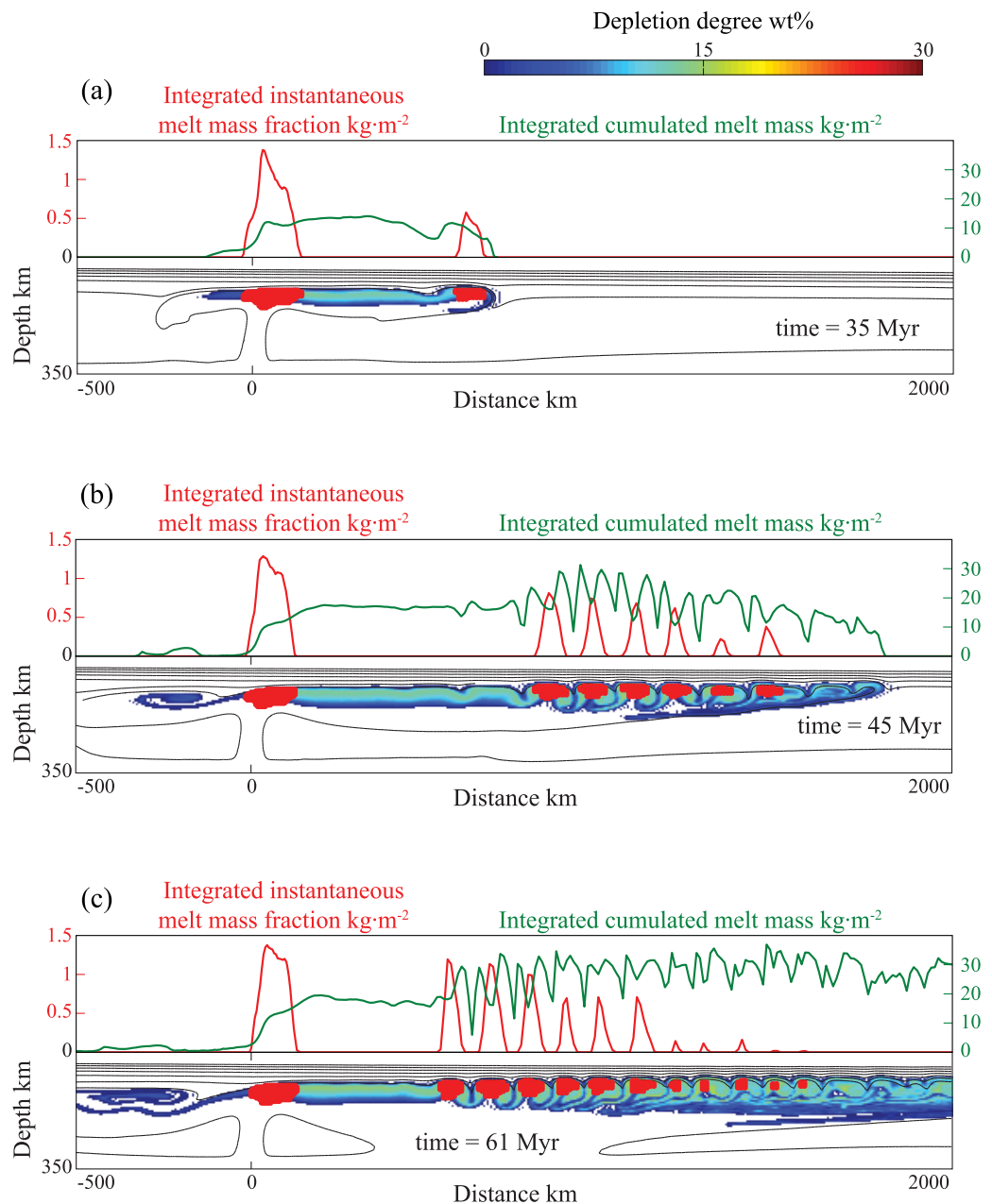


**Figure 2.** Evolution of the partial melting: melting domains, melt production, and depletion in simulation 17. (top) The total instantaneous melt mass (red line) and the depletion (accumulated melt mass, green line) integrated over vertical columns through the model. (bottom) The depletion degree field and the melting domains (red patches). Isotherms (black lines) are depicted from 800 to 1400°C in steps of 100°C.

further melting (Figure 2c). A quasi-steady-state, characterized by temporal variations of the average lithosphere thickness (depth of the 1300°C isotherm) in the last 2000 km of the domain (from the plume axis to the right side of the box) lower than 0.1%, is reached ~61 Myr after plume initiation for the moderate plume vigor modeled in simulation 17.

The discontinuous partial melting and progressive depletion structure modeled here may explain the spatial and temporal variations of magma production observed along hotspot tracks. This point has been extensively studied by *Ribe and Christensen* [1999] and *Bianco et al.* [2008], who interpreted these variations as the result of progressive extraction of different components in separated partial melting zones. We will therefore not detail this issue in the present article.

### 3.1. Definition of the Onset Time of SSC

The triggering of SSC in the lower part of a TBL has been shown to depend, for a temperature-dependent viscosity, on the structure of the unstable layer underlying the stagnant upper part of the TBL [Davaile and Jaupart, 1993]. Numerical and laboratory models demonstrated that the onset of SSC ( $\tau_c$ ) beneath a rigid lid depends on the Rayleigh number of the unstable layer ( $Ra_{SSC}$ ) and on the viscous dimensionless temperature scale ( $\theta$ ):  $\tau_c \propto Ra_{SSC}^{-2/3} \theta^\beta$ , where the exponent  $\beta$  depends on the modeled  $\theta$ -range [Dumoulin et al., 2005]. It may range from 8/3 [Choblet and Sotin, 2000], to 4/3 [Davaile and Jaupart, 1994], or  $\sim 0.7$  [Korenaga and Jordan, 2002, 2003; Huang et al., 2003]. The latter value corresponds to a Newtonian Arrhenius-type rheology and a  $\theta$ -range ( $\sim 5$ – $20$ ) consistent with the one expected for the mantle [Korenaga and Jordan, 2003; Huang et al., 2003].

Previous models [Moore et al., 1998; Thoraval et al., 2006; Agrusta et al., 2013] showed that the spreading of a mantle plume along the base of the lithosphere can switch an initially stable (or metastable) sublithospheric layer into an unstable state, triggering SSC, by increasing the temperature jump across the destabilized layer and, hence, by significantly increasing  $Ra_{SSC}$ . SSC triggering also depends on the ratio between plate and plume upwelling velocities. Slow plate or fast plume velocities promote a strong upstream flow that reduces the thickness of the unstable layer prior to its destabilization and delays the SSC onset in the downstream domain compared to fast plate or slow plumes cases, in which plume upstream flow is weak [Agrusta et al., 2013].

In the present study, we analyze the influence of partial melting on SSC dynamics by comparing the onset time of SSC in melt-dependent simulations to melt-free ones. All simulations are analyzed at a stage where quasi-steady state is reached. The horizontal location of plume impact,  $X_{impact}$ , is defined as the location of the maximum positive peak in vertical velocity, whereas the horizontal location of the first dripping instability,  $X_{onset}$ , is defined by the location of the first peak in vertical velocity downstream from the plume impact point (see supporting information Figures S1a and S1b for details). The onset time of SSC,  $\tau_c$ , is computed as the difference between  $X_{onset}$  and  $X_{impact}$  converted in time by dividing by  $V_{plate}$ :  $\tau_c = (X_{onset} - X_{impact}) / V_{plate}$ . Figure 3 shows two pairs of simulations with melt-free and melt-dependent physical properties for identical mantle viscosities ( $10^{21}$  Pa-s) and plate velocities ( $V_{plate} = 12.5$  cm-yr $^{-1}$ ), but different plume anomaly temperatures (300 and 350 K, simulations 20 and 22). Comparison of these two pairs of simulations shows that the feedbacks between partial melting and SSC dynamics are complex. Partial melting shifts the onset of SSC toward sensibly younger lithosphere ages (by  $\sim 2.5$  Myr) in simulation 20 ( $\Delta T_{plume} = 300$  K), whereas it has no meaningful influence on the SSC onset in simulation 22 ( $\Delta T_{plume} = 350$  K).

### 3.2. Dynamic Effects of Partial Melting on the SSC Onset Time

Analysis of full data set shows that the SSC onset in melt-dependent simulations may be accelerated, unchanged, or delayed relative to melt-free simulations. Melt-dependent simulations reveal a stronger time-dependence of the location of the SSC onset, implying larger error bars in the estimate of the SSC onset. As described below, the complex interplay between, on one hand, the negative feedback on SSC triggering produced by cooling due to the latent heat of melting, and, on the other hand, the positive feedback resulting from the buoyancy increase and the viscosity decrease associated with melting are likely to enlarge the domain where the TBL becomes unstable. We nevertheless think that this enhanced time-dependence does not have a strong influence on the SSC onset time.

As a consequence, we define an acceleration (delay) in the SSC onset if the SSC onset time of the melt-dependent simulation is lower (greater) than the melt-free one and if the two error bars do not overlap by more than half (Figure 4a). This definition corresponds to a minimum difference of 50 km in the ( $X_{onset} - X_{impact}$ ) distance between melt-free simulations and melt-dependent ones (see supporting information Table S1).

To quantify the convective regime in the sublithospheric layer, we define an internal thermal Rayleigh number,  $Ra_{thermal}^{SSC} = (\alpha g \rho_{sr} H^3 (T_{local} - T_0)) / (\kappa \mu_{local})$ , where  $\mu_{local}$  is the minimum viscosity and  $T_{local}$  is the corresponding temperature, averaged between  $X_{impact}$  and  $X_{onset}$  (cf. supporting information Figure S1c).  $Ra_{thermal}^{SSC}$  only considers the thermal effects on the sublithospheric layer buoyancy and viscosity. It does not include the additional buoyancy arising from melt retention and solid depletion nor the viscosity decrease due to melt retention. Figure 4b displays the variation of SSC onset time ( $\tau_c$ ) as a function of  $Ra_{thermal}^{SSC}$ . All melt-free cases (empty symbols) follow the power law relationship  $\tau_c = A (Ra_{thermal}^{SSC})^{-0.68}$  where  $A = 146.7$  [Agrusta et al., 2013]. However, most of the melt-dependent simulations (solid symbols in Figure 4b) deviate from

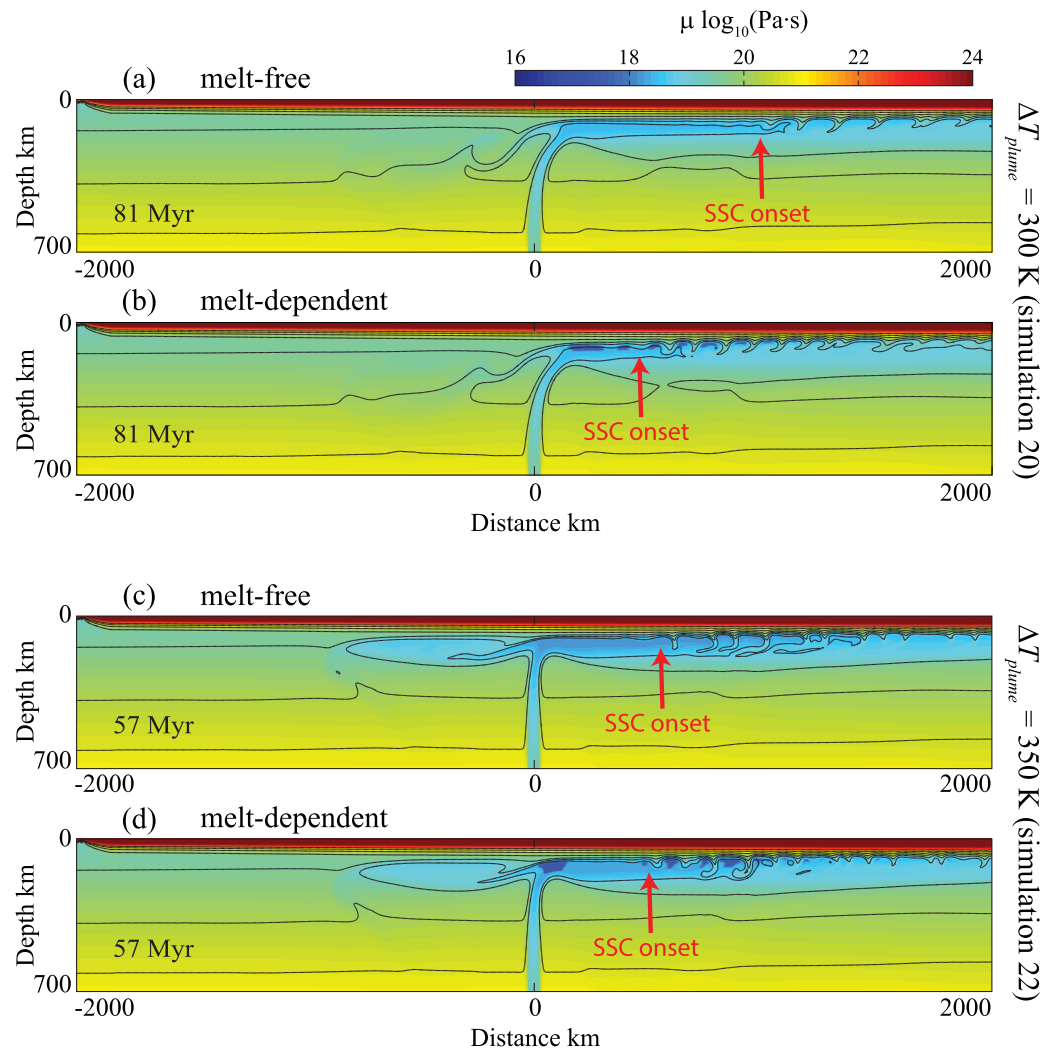


**Figure 3.** Comparison between (a, c) melt-free and (b, d) melt-dependent simulations for similar mantle viscosities ( $10^{21}$  Pa·s) and plate velocities ( $V_{plate} = 12.5$  cm·yr $^{-1}$ ), but different plume temperature anomalies: (a, b) 300 K and (c, d) 350 K. The color scale represents the viscosity field and the contour lines the isotherms from 1200 to 1800°C spaced by 100°C. Red arrows indicate the SSC onset.

this scaling law. In some simulations (circle symbols), the onset time is remarkably accelerated compared to melt-free simulations despite very similar  $Ra_{thermal}^{SSC}$  values. A constant  $Ra_{thermal}^{SSC}$  means that the thermal structure of the unstable layer is not notably modified, implying therefore that acceleration of the SSC onset time results from the buoyancy and/or viscosity variations ensuing from partial melting coupled to limited cooling by the loss of latent heat during melting. On the contrary, in simulations where the onset time of SSC remains more or less constant (diamond symbols) or is delayed (square symbols),  $Ra_{thermal}^{SSC}$  in the melt-dependent cases is lower than in the corresponding melt-free cases, indicating that temperature in the plume-fed layer decreases as a result of latent heat of melting (Figure 4c, see below). SSC delay indicates that this negative thermal effect is not overcome by buoyancy increase and/or viscosity decrease, whereas an unchanged SSC onset suggests that the two effects balanced each other.

To clarify the influence of the latent heat of melting on SSC dynamics, Figure 4c depicts the  $\tau_c - Ra_{thermal}^{SSC}$  relationship for simulations where the latent heat term (equation (2)) is not computed (solid symbols with black outlines). The simulations previously showing an unchanged or delayed SSC onset display an acceleration of the SSC onset when latent heat due to melting is turned off. This result is consistent with the increase of their  $Ra_{thermal}^{SSC}$  with respect to the corresponding cases that include latent heat effects. One exception (simulation 12) presents an unchanged SSC onset compared to the melt-free case. This behavior

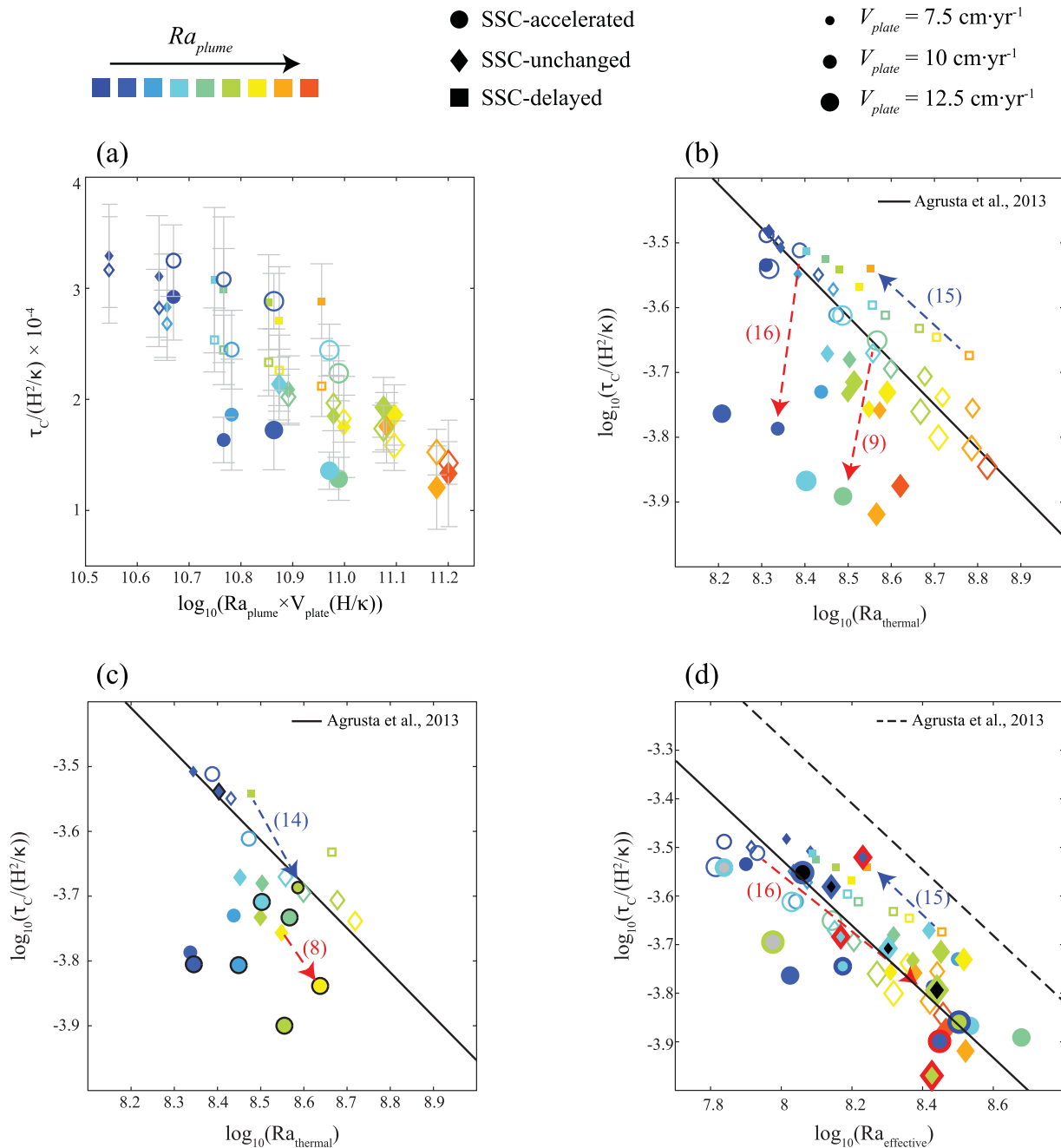


**Figure 4.** (a) Dimensionless onset time ( $\tau_c$ ) versus  $Ra_{plume} \times V_{plate} (H/\kappa)$ . The color scale highlights the plume vigor, cold colors represent weak plumes and hot colors represent strong plumes. Symbol sizes are proportional to plate velocities. Empty symbols indicate melt-free cases, filled symbols the dependent ones. The grey error bars are the standard deviation error for the  $\tau_c$ . (b)  $\tau_c$  versus  $Ra_{thermal}^{SSC}$ , the red arrows indicate two cases (simulations 9 and 16) for which the SSC onset is accelerated at roughly constant  $Ra_{thermal}^{SSC}$ ; the blue arrow highlights a case of SSC onset delay (simulation 15). The black line is the scaling relationship obtained by Agrusta et al. [2013]. (c)  $\tau_c$  versus  $Ra_{thermal}^{SSC}$  in simulations where the latent heat of melting (equation (2)) is switched off (symbols contoured in black). Melt-free (empty symbols) and full melt-dependent (solid symbols with no contour) simulations for the same conditions are shown for comparison. The blue arrow highlights the simulation 14, whose behavior changes from SSC-delay to SSC-acceleration when latent heat effects are neglected. The red arrow highlights simulation 8, where neglecting latent heat effects results in transition from a SSC-unchanged onset to SSC-acceleration. (d)  $\tau_c$  versus  $Ra_{effective}^{SSC}$ . The red and blue arrows indicate the same model pairs as in Figure 4b. The symbols with the red and blue outlines represent the melt-dependent cases with the age of the lithosphere at the plume impact of 20 Myr and 80 Myr, respectively. The symbols with the contour color following the  $Ra_{plume}$  color scale and filled in black and grey represent the melt-free cases performed for lithospheric ages at the plume impact point of 20 Myr and 80 Myr, respectively. The dashed black line is the scaling law by Agrusta et al. [2013] and the solid line is the same law calculated with  $Ra_{effective}^{SSC}$ .

may be explained by the low plate velocity ( $V_{plate} = 7.5 \text{ cm}\cdot\text{yr}^{-1}$ ) and the small plume thermal anomaly ( $\Delta T_{plume} = 300 \text{ K}$ ) in this simulation. The low plate velocity favors plume upstream flow, which tends to delay SSC triggering (see discussion below). In addition, the small thermal anomaly of the plume

( $Ra_{plume} = 2.63 \times 10^7$ ) produces limited melting and, hence a weak effect of latent heat on the temperature field.

The temperature reduction resulting from the latent heat of partial melting can be estimated by  $\Delta T_{latent} = (Q_L/C_p)\Delta M$ , and may be used to predict the effects of latent heat on  $Ra_{thermal}^{SSC}$ , then on the SSC onset time. For instance, for an initial temperature (before partial melting),  $T_{local}$ , of 1800 K at a depth  $Z_{local}$ , of 120 km, the temperature reductions due to latent heat loss associated with melting degrees of 5 wt % and 20 wt % are of 12 K and 48 K, respectively. These temperature decreases correspond respectively to viscosity increases by a factor of 1.13 and 1.63, respectively, and to a decrease in the buoyancy forces by a factor 0.98 and 0.96, respectively. Coupling the increase of viscous forces and decrease of buoyancy forces leads to a reduction of  $Ra_{thermal}^{SSC}$  of a factor of  $\sim 0.85$  and  $\sim 0.6$ , respectively, corresponding roughly to what we observed when latent heat is not modeled (Figure 4c).

A more precise description of the convective regime in the sublithospheric layer may be achieved using an effective Rayleigh number,  $Ra_{effective}^{SSC}$ , which takes into account the effects of partial melting on both buoyancy and viscosity, defined as:

$$Ra_{effective}^{SSC} = \frac{H^3 g}{\kappa \mu(Z_{local}, T_{local}, \phi)} \Delta \rho(Z_{local}, T_{local}, \phi, F) \quad (13)$$

where  $\Delta \rho(Z_{local}, T_{local}, \phi, F) = \rho_{sr} - \rho(Z_{local}, T_{local}, \phi, F)$  is the effective buoyancy difference. Density ( $\rho$ ) and viscosity ( $\mu$ ) are obtained from equations (9) and (10), respectively.  $T_{local}$  and  $Z_{local}$  are the temperature and depth corresponding to the minimum viscosity in the plume-fed layer, averaged between  $X_{impact}$  and  $X_{onset}$  (see supporting information Figure S1c).

When the SSC onset time is plotted against  $Ra_{effective}^{SSC}$  (Figure 4d), simulations roughly ( $R^2=0.48$ ) follow the power law relationship  $\tau_c = 82.2 (Ra_{effective}^{SSC})^{-0.68}$ , regardless whether partial melting is considered or not. The shift toward lower values of the proportionality constant between the scaling laws for  $Ra_{effective}^{SSC}$  and the  $Ra_{thermal}^{SSC}$  might result from the density increase with depth associated with the compressibility ( $\beta_s$ ) (equation (11)).

Melt-dependent simulations showing an accelerated SSC onset display higher  $Ra_{effective}^{SSC}$  relatively to their melt-free equivalents (red arrow in the Figure 4d), whereas for melt-dependent simulations in which the SSC onset is delayed relatively to the melt-free cases,  $Ra_{effective}^{SSC}$  is lower (blue arrow in the Figure 4d). Simulations in which SSC onset is unchanged exhibit similar  $Ra_{effective}^{SSC}$  for both melt-free and melt-dependent simulations.

For simplicity sake, in the present simulations, we used a linear Newtonian rheology (equation (9a)). There is significant evidence for a strain rate-dependent, nonlinear viscosity in the entire upper mantle [e.g., Ranalli, 2001; Mainprice et al., 2005; van Hunen et al., 2005]. Previous works suggest that the dynamics of convection in a system with a non-Newtonian rheology may be mimicked using a Newtonian rheology in which the activation enthalpy ( $H_a = E_a + PV_a$ ) in the dislocation creep law is divided by  $(n+1)/2 = 2$ , where  $n$  is the stress exponent in the dislocation creep law, if the effective viscosity is a function of the rate of dissipated energy (stress times strain rate) [Christensen 1984, Dumoulin et al., 1999]. Indeed, the dimensionless viscous temperature drop ( $\theta$ ) for a Newtonian viscosity defined using an activation enthalpy  $H_a/2$  is roughly the same as for a non-Newtonian rheology with  $n = 3$  and activation energy  $H_a$ . van Hunen et al. [2005] have shown that a higher reduction in the activation energy (by a factor close to 3.5) is necessary to reproduce, using a Newtonian rheology, the thermal evolution of the oceanic TBL modeled using a non-Newtonian rheology. However the aforementioned studies simulate a less complex situation than the present one and it is not possible to predict with precision the possible feedbacks between the effects of partial melting on the temperature field and physical properties that would be modeled in a non-Newtonian mantle.

### 3.3. Influence of Depletion-Induced Density Variations on SSC Onset

The depletion degree and the spatial distribution of the depleted residue also influence the SSC dynamics [Manglik and Christensen, 1997; Hernlund et al., 2008]. Figure 5a displays the depth of the upper limit of the depleted layer against the average depletion degree in the sublithospheric layer. The additional buoyancy related to solid depletion accelerates the onset of SSC only if the depletion degree is lower than 4 wt %. High melting degrees result in shallower and thicker depleted layers, which tend to inhibit the SSC

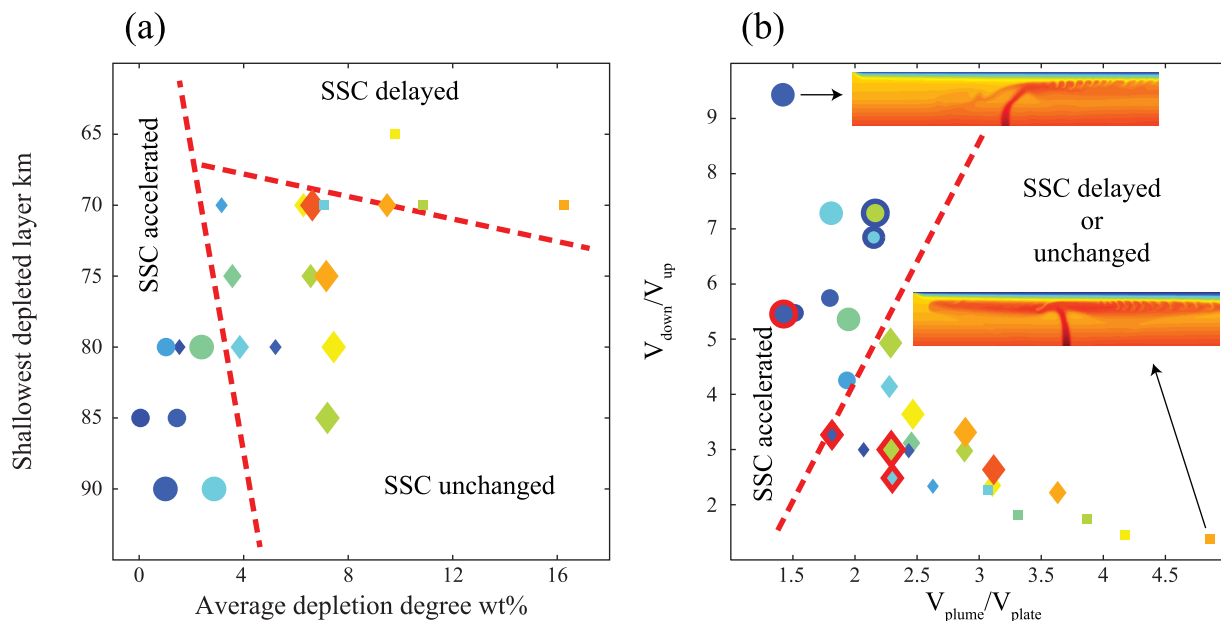


**Figure 5.** (a) Upper limit (depth) of the depleted layer versus the average depletion degree within the sublithospheric layer. The boundaries delimiting the three SSC onset regimes (red dashed lines) are largely arbitrary. Symbols colors and sizes refer to the legend depicted in Figure 4. (b) Regime diagram of plume spreading as a function of plate and plume velocities. The red dashed line discriminates simulations with SSC-onset acceleration from simulations with unchanged SSC or delayed SSC.

triggering. This observation is consistent with previous works that showed that if depletion is important and the depleted layer thick and rather shallow, the upper part of the unstable sublayer is likely to become too buoyant to be easily destabilized [Hernlund *et al.*, 2008; Sleep and Jellinek, 2008]. On the contrary, a thin depleted layer in the middle/lower part of the unstable layer enhances the density contrast between the top and bottom of the sublithospheric layer, favoring SSC [Jaupart *et al.*, 2007; Hernlund *et al.*, 2008].

In the present simulations, the depletion degree and the depleted layer thickness depend on how the plume spreads at the base of the moving lithosphere. The regime diagram proposed by Agrusta *et al.* [2013] to quantify the relative vigor of plume upstream and downstream flows based on the ratio of plume upwelling and plate velocities (Figure 5b) may thus be used to predict the variations in the SSC onset time resulting from partial melting. Significant acceleration of the SSC onset is expected for fast plate velocities and relatively weakly buoyant plumes. In these simulations, partial melting is moderate and only occurs downstream from the plume impact point. In contrast, highly buoyant plumes and/or slow plate velocities result in higher partial melting degrees in the vicinity of the plume impact point, strong latent heat-induced cooling, and the formation of an highly depleted layer. These processes inhibit acceleration of the SSC onset or may even delay it.

Note that, in the present simulations, we neglect partial melting occurring below the ridge. Models considering the effect of partial melting on buoyancy and viscosity proposed that melting at the ridge results in the formation of a 60–70 km-thick dehydrated and refractory harzburgite layer [Hirth and Kohlstedt, 1996], which may stabilize the lithosphere, inhibiting the penetration of SSC [Ballmer *et al.*, 2009; Afonso *et al.*, 2008]. Based on equation (5) we estimate that, in the present simulations, partial melting at the ridge would generate a refractory harzburgite layer, that may extend up to  $\sim 50$  km depth. This layer would be too shallow to interact with the plume-induced SSC in any of the models that predict acceleration of the SSC onset, which are all characterized by SSC concentrated in a deep and thin plume-fed layer. In models with slow plates and/or vigorous plumes, but also for young lithosphere ages at the plume impact point, the SSC might interact with the ridge-formed refractory layer. These simulations already show high degrees of partial melting that inhibit the SSC onset. The extra buoyancy of the shallow refractory lithosphere would only further hinder the SSC onset. We can therefore infer that the depletion of the shallow lithospheric mantle melting at the ridge should not alter our predictions of the influence of partial melting on the dynamics of the SSC in the plume-fed layer.

### 3.4. Influence of the Age of the Lithosphere at the Plume Impact Point

To investigate the possible influence of the lithospheric structure at the impact point on the dynamics of SSC, 12 simulations were performed, in melt-free and melt-dependent conditions, where the age of the lithosphere at the plume impact point was either 20 Myr or 80 Myr, instead of 40 Myr (Table 2). The other parameters are identical to those of simulations 17 (plate velocity of  $10 \text{ cm}\cdot\text{yr}^{-1}$  and plume anomaly of 325 K) and 22 (plate velocity of  $12.5 \text{ cm}\cdot\text{yr}^{-1}$  and plume anomaly of 350 K), both presenting unchanged SSC onsets between melt-free and melt-dependent simulations. For the 20 Myr old plate case, we also run simulations similar to cases 16 and 20 (plume anomaly of 300 K and plate velocity of  $10 \text{ cm}\cdot\text{yr}^{-1}$  or  $12.5 \text{ cm}\cdot\text{yr}^{-1}$ , respectively), which exhibit an acceleration of the SSC onset when partial melting effects are included. We do not discuss the equivalent simulations for a 80 Myr old plate at the plume impact point, because at such high plate velocities a 300 K plume anomaly is too weak to trigger partial melting below a thick lithosphere.

The lithosphere age affects the plume spreading. Plumes impacting a young and thin lithosphere tend to display a stronger upstream flow compared to those impacting an old and thick lithosphere (Figure 5d). This behavior may be related to the depth-dependence of the viscosity, which leads to higher viscosities at the lithosphere base for plumes impacting older lithospheres and, as a consequence, to a likely stronger kinematic coupling between the plate and plume material. The variation in the onset time of the SSC arising from partial melting displays the same dependence on the plume spreading dynamics as discussed in section 3.3. Melt-dependent simulations presenting a high  $V_{\text{down}}/V_{\text{up}}$  ratio display an accelerated triggering of SSC relatively to melt-free cases (simulations 20a20, 17a80, 22a80), whereas simulations with low  $V_{\text{down}}/V_{\text{up}}$  ratios exhibit unchanged SSC onset times (simulations 16a20, 17a20 and 22a20) (Figure 4d).

### 3.5. Influence of the Critical Melt Fraction, $\phi_c$

In this study, the amount of melt retention controls both viscosity and density variations in the partially molten domains. We tested the effect of the liquid extraction threshold,  $\phi_c$ , by varying its value between 0.5 and 5% in a simulation showing a clear acceleration of the SSC onset (simulation 16). To constrain the respective influence of viscosity and density dependences in melt fraction, we run for the different  $\phi_c$  extra simulations where the melt retention affects only the viscosity or the density (Table 2). Figure 6a highlights that the melt retention-induced density reduction has a strong influence on SSC dynamics, explaining the acceleration of the onset of SSC in most cases. In contrast, despite a reduction in viscosity by up to two orders of magnitude in the domains where melting occurs, the melt-induced reduction in viscosity alone (red line in Figure 6a) does not result in significant acceleration in the onset of the SSC. Mechanical weakening associated with retained melt fraction contributes, however, to the acceleration of the SSC onset when the buoyancy is also melt-dependent and if  $\phi_c$  is larger than 1% (viscosity reduction at least equal to 10, equation (9)). The weak influence of the viscosity reduction on the SSC dynamics may be explained by the small volumes in which it is effective. Indeed, for a  $\phi_c$  of 1%, melt-induced viscosity reduction only occurs in domains that are actively melting, that is, in the plume impact area and the SSC upwelling branches (Figure 3). Higher melt extraction thresholds allow for enlarged domains of melt-related viscosity reduction and, hence, for a stronger influence on the SSC dynamics.

The relative effects of temperature, solid depletion, and melt retention on buoyancy are depicted in Figure 6b. Compositional effects (melt retention and depletion of the residue) are much stronger than thermal ones for all liquid extraction thresholds. Even for realistic melt extraction thresholds ( $\phi_c = 1\%$ ), the buoyancy increase due to melt retention is higher than the one induced by a  $50^\circ\text{C}$  temperature increase in the peridotite. Moreover, for high retained melt fractions ( $>3.5\%$ ), the buoyancy increase due to melt retention may also exceed the one related to depletion.

### 3.6. Compositional Stratification in the Plume-Fed Sublithospheric Layer

Partial melting yields compositional variations in the plume-fed sublithospheric layer. The internal structure of this layer away from the plume axis is controlled by the interactions between the large-scale flow (plate tectonic scale), the melt production, and the SSC. The large-scale flow (plume head spreading and/or dragging by the plate motion) advects horizontally the refractory residues that form in response to partial melting, leading to compositional stratification. SSC, on the other hand, produces vertical motions, which mix and recycle melting residues. However, the buoyancy of the melting residues tends to counteract homogenization. Under specific conditions, these complex interactions are likely to induce compositional layering,

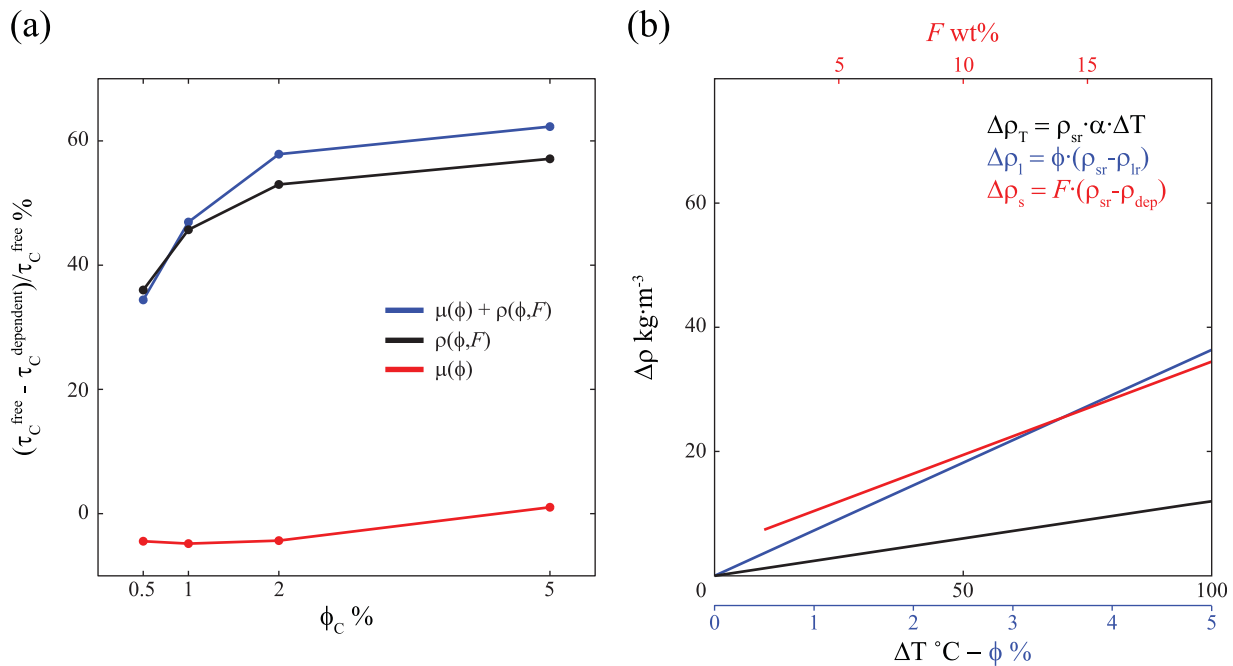


**Figure 6.** (a) Variations in the SSC onset time in simulation 16 as a function of the melt extraction threshold. Three kinds of simulation are displayed: (1) both density and viscosity depend on the retained melt fraction and the density also depends on depletion of the solid residue (blue line); (2) partial melting only affects the density (both melt retention and depletion effects are considered, black line); (3) partial melting and melt retention only affect the viscosity (red line). (b) Buoyancy change due to variations in temperature of the solid peridotite (by up to 100°C), solid depletion (up to 20 wt %), and melt retention (up to 5% porosity).

which may be preserved upon cooling as the plate moves away from the plume axis, as proposed for the Ontong Java Plateau lithosphere [Ishikawa *et al.*, 2004; Tommasi and Ishikawa, 2014].

The present model shows that the geometry of the large-scale flow plays a major role in the formation of compositional stratification within the convecting sublithospheric plume fed layer. Simulations characterized by a Poiseuille-like large-scale flow in the sublithospheric layer, that is, those in which the plume material moves downstream faster than plate velocity ( $V_{\text{plate}}/V_{\text{down}} < 1$ , Figure 7a), are characterized by compositional mixing in the plume-fed layer. On the contrary, in simulations characterized by a Couette-like flow in the plume-fed layer, that is, in which plume material is predominantly dragged by plate motion ( $V_{\text{plate}}/V_{\text{down}} > 1$ , Figure 7a), the most refractory peridotitic material seems to concentrate at shallow levels just below the lithosphere, leading to development of a stratification in the depletion degree. High plate velocities (Figure 7b) and/or low plume vigor (Figure 7c) may therefore promote compositional stratification.

### 3.7. Thermo-Mechanical Erosion of the Lithosphere and Deviation From the Half-Space Cooling Model

SSC increases the heat flux at the base of the lithosphere. It is responsible for lithospheric thinning by convective removal of the base of the rigid lid and increased conductive heating within it [Doin and Fleitout, 1996; Dumoulin *et al.*, 1999]. To estimate the lithosphere erosion by SSC in the plume-fed sublithospheric layer, we analyzed the topography of the base of the lithosphere, which may be defined by an isotherm,  $T_{\text{LAB}}: T_{\text{LAB}} = T_{\text{local}} - 2.24\Delta T_{\mu}$ , where  $\Delta T_{\mu} = (d \ln(\mu)/dT)^{-1} = (T_1 - T_0)\theta^{-1}$  is the rheological temperature scale [Davaille and Jaupart, 1993]. In the present simulations  $2.24\Delta T_{\mu}$  ranges from 200 to 250 K and  $T_{\text{LAB}}$  from 1300 to 1380°C. We chose to use the lower value of 1300°C to define the base of the lithosphere. Figure 8a displays the shallowest depth of this isotherm as a function of the horizontal distance to the plume impact point for all simulations. The minimum depth of the LAB does not vary significantly between melt-free cases (empty symbols) and melt-dependent ones (solid symbols). However, the location of the shallowest LAB relative to the plume impact point may change markedly. It is closer to the plume impact point for simulations presenting a faster SSC onset, and farther away for simulations where SSC onset is delayed. Note that the location of the shallowest LAB is different from the onset point of SSC (see supporting information Tables

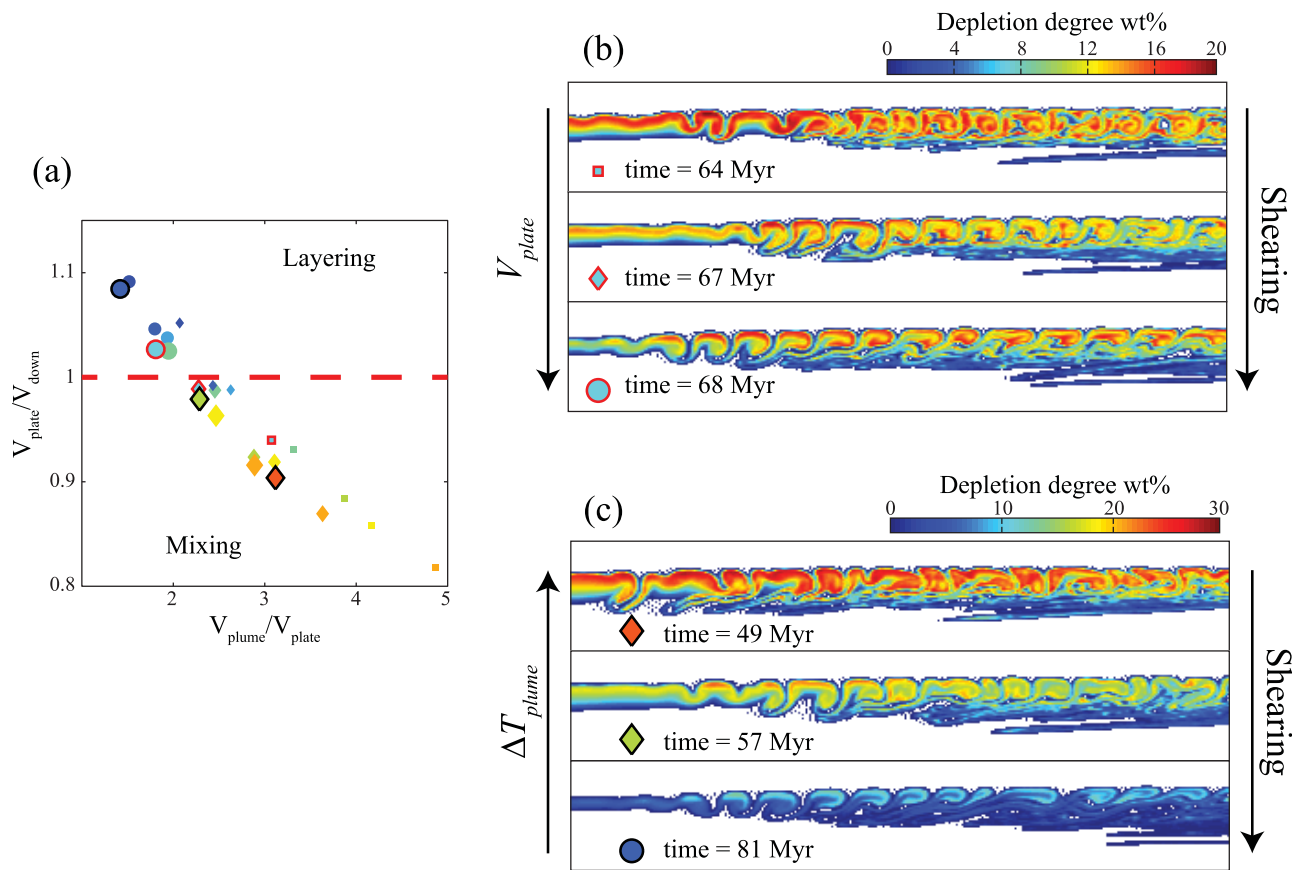


**Figure 7.** (a) Shearing intensity in the sublithospheric layer ( $V_{plate}/V_{down}$ ) as a function of the ratio  $V_{plume}/V_{plate}$ . Compositional stratification is observed for simulations with  $V_{plate}/V_{down} > 1$ . As in Figure 4, symbols color and size indicate plume vigor and plate velocities. (b) Compositional stratification promoted by increasing plate velocity (red contoured symbols in Figure 7a). (c) Compositional stratification promoted by reducing plume vigor (black contoured symbols in Figure 7a). Close-up on the plume-fed convecting layer far away from the plume impact point, from 400 to 2000 km from the plume axis.

S1 and S5). Far away from the plume impact, the thermal structure of the lithosphere in melt-dependent simulations is very similar to the one observed in melt-free ones (Figures 8b and 8c).

To estimate the lithosphere rejuvenation related to plume-induced SSC, we study how the thermal structure of the lithosphere deviates from the half-space cooling (HSC) model by computing the apparent thermal age ( $t_a$ ) of the lithosphere. The lithospheric apparent thermal age is the age that would lead to the same temperature structure as the one produced by the cooling of the lithospheric TBL following the HSC-model [Ritzwoller *et al.*, 2004].  $t_a$  is computed, first, by averaging the lithosphere temperatures on a depth interval ranging from the surface to 100 km depth, and, second, using the HSC model, by calculating the lithosphere apparent thermal age [van Hunen *et al.*, 2005]. We then compare this apparent thermal age,  $t_a$ , to the actual age of the lithosphere,  $t_r$ , for simulations with a plate velocity of  $12.5 \text{ cm}\cdot\text{yr}^{-1}$  and  $7.5 \text{ cm}\cdot\text{yr}^{-1}$ , respectively (Figures 8d and 8e). This comparison reveals that: (i) the lithosphere is rejuvenated upstream from the plume impact point for all simulations presenting a strong upstream flow (vigorous plumes and/or slow plate velocities); (ii) at plume impact the apparent age is lower than the actual age in all simulations, but the lithosphere rejuvenation lasts less than 10 Myr for fast plate velocities and/or weak plumes (Figure 8d) and less than 5 Myr for slow plates and/or strong plumes (Figure 8e); (iii) after this rejuvenation period the apparent lithosphere age increases again following the slope of the HSC-model. Melt-dependent cases show a shift of stage (iii) toward younger ages for simulations characterized by an acceleration of the SSC onset, but they do not depict a significant enhancement of the intensity of the lithosphere rejuvenation (Figure 8d).

Moreover, plume spreading and associated SSC influence only the thermal state of the deep lithosphere. Indeed, if apparent thermal ages are calculated by averaging temperature in the first 50 km of the plate, instead of 100 km, the deviation from HSC-model vanishes, indicating that the top 50 km of the plate are

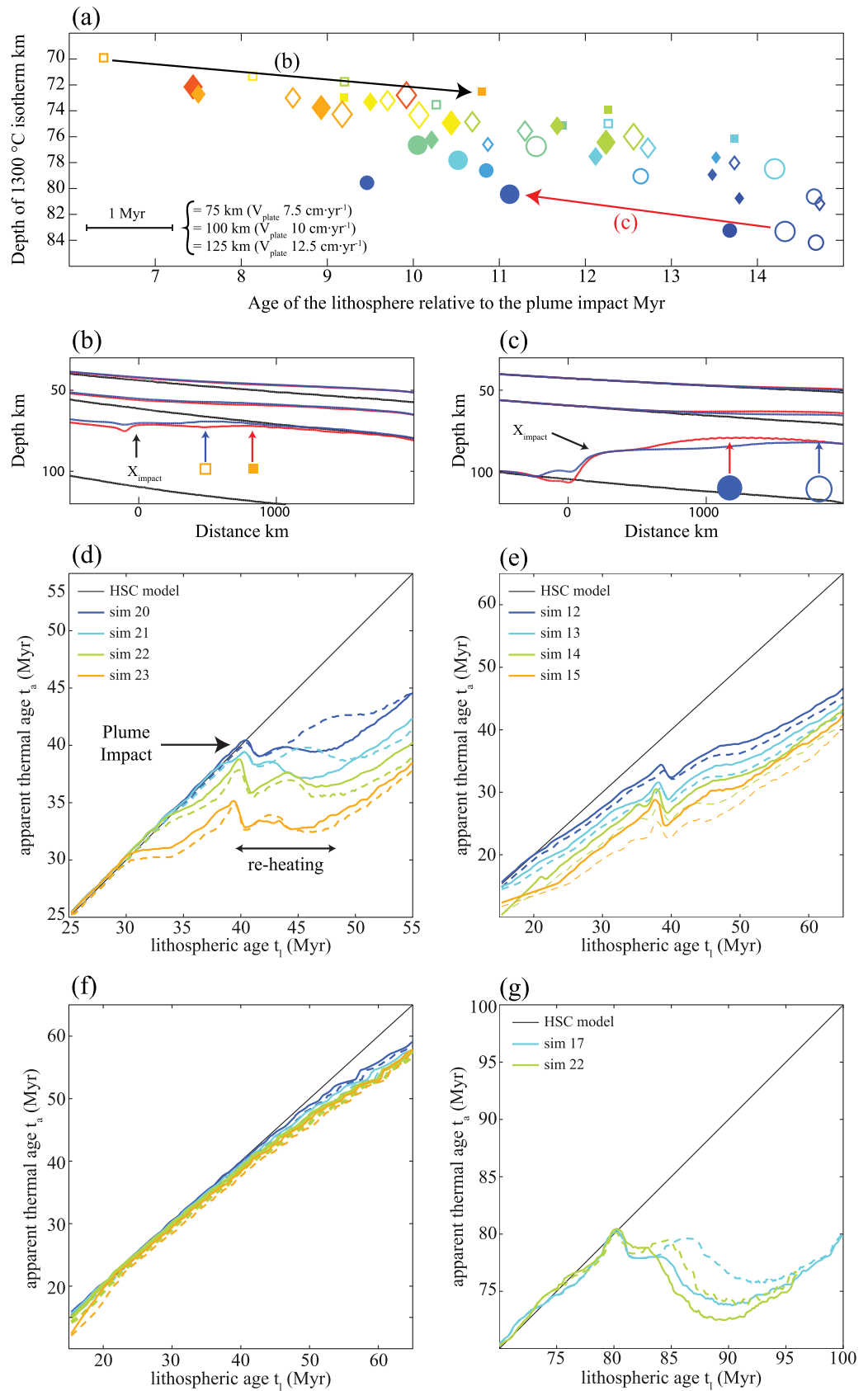


Figure 8.

not sensitive to the plume-lithosphere interactions. The maximum age deviation of  $\sim 5$  Myr is observed  $\sim 20$  Myr after plume impact for a vigorous plume impacting a slow plate ( $V_{\text{plate}} = 7.5 \text{ cm}\cdot\text{yr}^{-1}$ ; Figure 8f).

Analysis of thermal rejuvenation simulated for the case in which a 325 K anomaly plume impacts a fast plate aged of 80 Myr at the impact point (simulation 17) predicts a clear rejuvenation by ca. 10 Myr at 500 km away from the plume impact point (cyan lines, Figure 8g). This result is consistent with the thermal rejuvenation of the Pacific lithosphere beneath Hawaii inferred from geophysical observations [Ritzwoller *et al.*, 2004].

#### 4. Discussion: Limitations of the Present Model

The models presented in this paper allow for evaluating how partial melting, via its influence on the temperature field (latent heat) and on the upper mantle density and viscosity, affects the dynamics of the small-scale convection occurring in the plume-fed sublithospheric layer beneath a fast moving plate. The effect of partial melting on the viscosity of the solid residue through depletion in water [Karato *et al.*, 1986] is not considered in this study, where an initially dry and fertile mantle is assumed. A more accurate partial melting simulation would notably require the implementation of (1) the water effect on the peridotite melting process, (2) a follow-up of the water exchanges between melt and solid peridotite, as well as (3) a viscosity dependent on the peridotite hydration. Recent experimental data nonetheless suggest that the water-weakening effect on peridotite rheology might be much lower than previously proposed: a factor 2–3 rather than 100 [Demouchy *et al.*, 2012; Girard *et al.*, 2013; Fei *et al.*, 2013], implying that hydrolytic weakening may have minor consequences. In addition, recent data on mantle xenoliths from the Ontong Java mantle root show rather high hydrogen contents in olivine from highly refractory harzburgites, suggesting that the mantle lithosphere atop a plume may be rehydrated by percolating melts or fluids [Demouchy *et al.*, 2015]. If these recent data, which point to a weak effect of dehydration by partial melting on the upper mantle viscosity are correct, then the model predictions should not be significantly changed by implementing the viscosity dependence in water content. If, on the other hand, the peridotite viscosity strongly increases during dehydration associated with partial melting, we may speculate about the possible consequences as a function of already published studies [Afonso *et al.*, 2008; Ballmer *et al.*, 2009, 2011; Kaislaniemi and van Hunen, 2014]. For a hydrous mantle, partial melting will start at deeper levels, but the first partial melting event is likely to dry out the peridotites and the system will then behave as a dry one [Katz *et al.*, 2003]. In our model this would produce a first decrease in temperature within the plume material at deeper levels (due to latent heat). It would also strengthen the depleted and dehydrated residues relative to the unmolten peridotite. Depending on the strength of the viscosity increase associated with partial melting (which is presently poorly constrained as discussed above), this might or not further stabilize the TBL and hence hinder the SSC. If the effect of dehydration on the rheology is strong, probably SSC will be delayed in a larger range of conditions than what is predicted by the present ‘dry peridotite’ model.

The instantaneous numerical melt extraction as soon as a critical melt extraction threshold is exceeded, used here to prevent the accumulation of unrealistic melt fractions, is also an extreme oversimplification. A large body of evidence, mainly from studies of peridotite massifs [Le Roux *et al.*, 2007, 2008; Soustelle *et al.*, 2009; Higgie and Tommasi, 2012, 2014] argues for porous flow of melts, melt-rock reactions, and for strong feedbacks between deformation and melt distribution in the upper mantle. Such feedbacks are also evidenced in two-phase models [Connolly and Podladchikov, 2007; Bouilhol *et al.*, 2011]. By assuming an instantaneous melt extraction, we neglect the possible effects of melt percolation and the possible viscosity

**Figure 8.** (a) Distance (converted in time) between plume impact point and the location where the 1300°C isotherm is the shallowest. (b, c) 900°C, 1100°C, and 1300°C isotherms (averaged over the quasi steady state time window), for simulations showing (b) an increased distance and (c) a reduced distance between the minimum depth of the 1300°C isotherm and the plume impact point. Black lines represent the lithosphere state at equilibrium (without plume), red lines the melt-dependent model, and blue lines the melt-free model. Arrows indicate the location of the minimum depth of the 1300°C isotherm in each case. (d) Apparent thermal age ( $t_a$ ) versus lithospheric age ( $t_l$ ), for a set of models in which the plate moves at  $12.5 \text{ cm}\cdot\text{yr}^{-1}$  (simulations 20–23). Solid lines represent melt-dependent cases while the dashed lines are the melt-free cases. The arrow indicates the plume impact point at 40 Myr. The horizontal segment shows the reheating period (ii). (e)  $t_a$  versus  $t_l$  for a set of simulations where the lithosphere velocity is  $7.5 \text{ cm}\cdot\text{yr}^{-1}$  (simulations 12–15). (f)  $t_a$  versus  $t_l$ , for the same set of simulations as in Figure 8d, if plate temperatures are averaged on the first shallow 50 km. (g)  $t_a$  versus  $t_l$ , for a lithosphere 80 Myr old at the impact point location, for simulation 17 ( $V_{\text{plate}} = 10 \text{ cm}\cdot\text{yr}^{-1}$  and  $\Delta T_{\text{plume}} = 325 \text{ K}$ ) and for simulation 22 ( $V_{\text{plate}} = 12.5 \text{ cm}\cdot\text{yr}^{-1}$  and  $\Delta T_{\text{plume}} = 350 \text{ K}$ ).

reduction at the base of the lithosphere, but also the effects of melt crystallization during ascent, which should affect the temperature structure (heating by release of latent heat of crystallization) and the changes density field of the base of the lithosphere, since melt rock reactions may result in iron enrichment and, hence, in density increase in the peridotites [Tommasi *et al.*, 2004].

Last, but not least, the simulations performed in this study are restricted to two dimensions. Passing from 2-D to 3-D strongly modifies the SSC geometry. In 3-D, shearing caused by plate motion favors SSC convection rolls parallel to the plate velocity (longitudinal rolls) relative to those oriented perpendicular to the plate motion (transversal rolls [Richter, 1975]). Nevertheless, the onset of SSC has been proven to be independent of the third dimension [Huang *et al.*, 2003; van Hunen *et al.*, 2003]. The scaling laws developed in 2-D may thus also apply in 3-D [Davaille and Jaupart, 1994; Dumoulin *et al.*, 2005; Huang *et al.*, 2003; van Hunen *et al.*, 2003]. However, 3-D effects cannot be neglected regarding the dynamics of the large-scale plume-lithosphere interaction. Three-dimensional models show that the plume material spreads out not only in the direction of the plate motion but also laterally, forming a parabolic shape elongated in the direction of plate velocity [Ribe and Christensen, 1994; Moore *et al.*, 1998; Ballmer *et al.*, 2011]. This 3-D spreading largely reduces the upstream flow. Without running full 3-D calculations, we may only speculate on how 3-D should change the  $V_{up}/V_{down}$  ratio and, consequently, the regime diagram in Figures 5 and 7. As plume downstream flow is probably enhanced in 3-D, and since it favors an earlier SSC onset, in 3-D partial melting might result in acceleration of the onset of SSC for a wider range of plume anomalies (hotter plumes) and/or plate velocities (lower plate speeds).

## 5. Conclusions

In spite of the limitations discussed above, the simulations presented in this article show that partial melting does modify the SSC dynamics in the plume-fed convecting sublithospheric layer. They also highlight a complex interplay between large-scale flow (plate tectonics scale) and low-wavelength convective deformation. Indeed the interactions between: (1) cooling induced by the latent heat of melting, (2) buoyancy increase in both partially molten rocks and solid depleted residues, and (3) viscosity reduction in actively melting regions, which yield acceleration, no-change, or even delay of the SSC onset relative to melt-free cases, are strongly influenced by plume-lithosphere interactions at larger scales. The kinematics of the large-scale flow in the plume-fed material, which is controlled by the ratio between plume upwelling and plate velocities, has a strong effect on whether the SSC onset is accelerated or delayed by partial melting, via its influence on the plate thickness and on the melting behavior.

Melt-dependent simulations do not follow an exponential relationship between the onset time of the SSC ( $\tau_c$ ) and the  $Ra_{thermal}^{SSC}$  that includes only thermal effects on the buoyancy. A power law relationship with an exponent of  $-2/3$  is nevertheless verified when the convecting layer is characterized using  $Ra_{effective}^{SSC}$ , which also includes viscosity and density reductions due to partial melting. Melt-dependent simulations showing acceleration of the SSC onset correspond to higher  $Ra_{effective}^{SSC}$  and almost identical  $Ra_{thermal}^{SSC}$ , whereas those in which SSC is delayed correspond to  $Ra_{effective}^{SSC}$  and  $Ra_{thermal}^{SSC}$  lower than for their corresponding melt-free simulations. The SSC onset therefore occurs earlier when the reduction in density and, to a lesser extent, in viscosity, induced by partial melting is high enough to overcome the cooling effect in the plume-fed layer resulting from latent heat of melting. SSC-delayed simulations systematically exhibit high degrees of melting, and, consequently, strong cooling by latent heat of melting. For instance, production of 20 wt % of melt at the plume head corresponds to a reduction in temperature of  $\sim 40^\circ\text{C}$ . This temperature decrease produces a relative increase density of  $\sim 0.2\%$ , and a viscosity increase by a factor  $\sim 1.5$  in the plume-fed sublithospheric layer.

Despite a viscosity reduction by up to two orders of magnitude in the partially molten pockets, the viscosity decrease has no dominant influence on SSC dynamics, as it is restricted to the actively melting areas. The main ingredient accelerating SSC dynamics is the increase in buoyancy forces, due to both melt retention and depletion of the solid residue. However, SSC acceleration only occurs at moderate melt production, because at high degrees of melting, the temperature decrease due to latent heat of melting and the development of a thick buoyant depleted layer at the base of the lithosphere tend to inhibit SSC. This depletion stratification is controlled by the plume vigor and plate velocity, being favored beneath fast moving plates.

Early development of SSC due to partial melting does not result in more efficient thinning and thermal rejuvenation of the lithosphere. However, it affects the location of the shallowest LAB (which ranges between 72 and 82 km depth in the present simulations) relative to the plume impact point. Acceleration (delay) of the SSC leads to maximum shallowing of the LAB closer to (farther from) the plume impact point by up to 375 km.

### Acknowledgments

The research leading to these results has been funded by the Initial Training Network (ITN) Crystal2Plate, an FP7-funded Marie Curie Action under grant agreement PITN-GA-2008-215353. It has also been supported by NERC (grant NE/J008028/1) and made use of the facilities of N8 HPC provided and funded by the N8 consortium and EPSRC (grant EP/K000225/1). The N8 HPC is coordinated by the Universities of Leeds and Manchester. We thank E. Mittelstaedt, the Editor T. Becker and two anonymous reviewers for their valuable suggestions. The authors would like to thank Valentina Magni and Lars Kaislaniemi for useful discussions. Data for this paper can be made available upon request from the authors.

### References

- Abouchami, W., A. W. Hofmann, S. J. G. Galer, F. A. Frey, J. Eisele, and M. Feigenson (2005), Lead isotopes reveal bilateral asymmetry and vertical continuity in the Hawaiian mantle plume, *Nature*, *434*(7035), 851–856.
- Afonso, J. C., S. Zlotnik, and M. Fernández (2008), The effects of compositional and rheological stratifications on small-scale convection under the oceans: Implications for the thickness of oceanic lithosphere and seafloor flattening, *Geophys. Res. Lett.*, *35*, L20308, doi:10.1029/2008GL035419.
- Agrusta, R., D. Arcay, A. Tommasi, A. Davaille, N. Ribe, and T. Gerya (2013), Small-scale convection in a plume-fed low-viscosity layer beneath a moving plate, *Geophys. J. Int.*, *194*, 591–610, doi:10.1093/gji/ggt128.
- Ballmer, M. D., J. van Hunen, G. Ito, T. A. Bianco, and P. J. Tackley (2009), Intraplate volcanism with complex age–distance patterns—A case for small-scale sublithospheric convection, *Geochem. Geophys. Geosyst.*, *10*, Q06015, doi:10.1029/2009GC002386.
- Ballmer, M. D., G. Ito, J. van Hunen, and P. J. Tackley (2011), Spatial and temporal variability in Hawaiian hotspot volcanism induced by small-scale convection, *Nat. Geosci.*, *4*(7), 457–460.
- Bianco, T. A., G. Ito, J. van Hunen, M. D. Ballmer, and J. J. Mahoney (2008), Geochemical variation at the Hawaiian hot spot caused by upper mantle dynamics and melting of a heterogeneous plume, *Geochem. Geophys. Geosyst.*, *9*, Q11003, doi:10.1029/2008GC002111.
- Bianco, T. A., G. Ito, J. van Hunen, M. D. Ballmer, and J. J. Mahoney (2011), Geochemical variations at intraplate hot spots caused by variable melting of a veined mantle plume, *Geochem. Geophys. Geosyst.*, *12*, Q0AC13, doi:10.1029/2011GC003658.
- Bouilhol, P., J. A. D. Connolly, and J.-P. Burg (2011), Geological evidence and modeling of melt migration by porosity waves in the sub-arc mantle of Kohistan (Pakistan), *Geology*, *39*(12), 1091–1094.
- Byrnes, J. S., E. E. Hoof, D. R. Toomey, D. R. Villagómez, D. J. Geist, and S. C. Solomon (2015), An upper-mantle seismic discontinuity beneath the Galápagos Archipelago and its implications for studies of the lithosphere-asthenosphere boundary, *Geochem. Geophys. Geosyst.*, *16*, 1070–1088, doi:10.1002/2014GC005694.
- Cadio, C., M. D. Ballmer, I. Panet, M. Diament, and N. Ribe (2012), New constraints on the origin of the Hawaiian swell from wavelet analysis of the geoid to topography ratio, *Earth Planet. Sci. Lett.*, *359–360*, 40–54.
- Choblet, G., and C. Sotin (2000), 3D thermal convection with variable viscosity: Can transient cooling be described by a quasi-static scaling law?, *Phys. Earth Planet. Inter.*, *119*(3–4), 321–336.
- Christensen, U. (1984), Convection with pressure- and temperature-dependent non-Newtonian rheology, *Geophys. J. R. Astron. Soc.*, *77*, 343–384.
- Christensen, U. R., and D. A. Yuen (1985), Layered convection induced by phase transitions, *J. Geophys. Res.*, *90*(B12), 10,291–10,300.
- Connolly, J. A. D., and Y. Y. Podladchikov (2007), Decompaction weakening and channeling instability in ductile porous media: Implications for asthenospheric melt segregation, *J. Geophys. Res.*, *112*, B10205, doi:10.1029/2005JB004213.
- Crough, S. T., and D. M. Jurdy (1980), Subducted lithosphere, hotspots, and the geoid, *Earth Planet. Sci. Lett.*, *48*(1), 15–22.
- Davaille, A., and C. Jaupart (1993), Transient high-Rayleigh-number thermal convection with large viscosity variations, *J. Fluid Mech.*, *253*, 141–166.
- Davaille, A., and C. Jaupart (1994), Onset of thermal convection in fluids with temperature-dependent viscosity: Application to the oceanic mantle, *J. Geophys. Res.*, *99*(B10), 19,853–19,866.
- Demouchy, S., A. Tommasi, F. Barou, D. Mainprice, and P. Cordier (2012), Deformation of olivine in torsion under hydrous conditions, *Phys. Earth Planet. Inter.*, *202–203*, 56–70.
- Demouchy, S., A. Ishikawa, A. Tommasi, O. Alard, S. Keshav (2015), Characterization of hydration in the mantle lithosphere: Peridotite xenoliths from the Ontong Java Plateau as an example, *Lithos*, *212*, 189–201.
- Doin, M. P., and L. Fleitout (1996), Thermal evolution of the oceanic lithosphere: An alternative view, *Earth Planet. Sci. Lett.*, *142*(1–2), 121–136.
- Dumoulin, C., M.-P. Doin, and L. Fleitout (1999), Heat transport in stagnant lid convection with temperature- and pressure-dependent Newtonian or non-Newtonian rheology, *J. Geophys. Res.*, *104*(B6), 12,759–12,777.
- Dumoulin, C., M. P. Doin, D. Arcay, and L. Fleitout (2005), Onset of small-scale instabilities at the base of the lithosphere: Scaling laws and role of pre-existing lithospheric structures, *Geophys. J. Int.*, *160*(1), 344–356.
- Farnetani, C., and M. Richards (1994), Numerical investigations of the mantle plume initiation model for flood basalt events, *J. Geophys. Res.*, *99*(B7), 13,813–13,833.
- Farnetani, C., and M. Richards (1995), Thermal entrainment and melting in mantle plumes, *Earth Planet. Sci. Lett.*, *136*(3–4), 251–267.
- Faul, U. H. (2001), Melt retention and segregation beneath mid-ocean ridges, *Nature*, *410*(6831), 920–923.
- Faul, U. H., and I. Jackson (2007), Diffusion creep of dry, melt-free olivine, *J. Geophys. Res.*, *112*, B04204, doi:10.1029/2006JB004586.
- Fei, H., M. Wiedenbeck, D. Yamazaki, and T. Katsura (2013), Small effect of water on upper-mantle rheology based on silicon self-diffusion coefficients, *Nature*, *498*(7453), 213–215.
- Gerya, T. V., and D. A. Yuen (2003), Characteristics-based marker-in-cell method with conservative finite-differences schemes for modeling geological flows with strongly variable transport properties, *Phys. Earth Planet. Inter.*, *140*(4), 293–318.
- Girard, J., J. Chen, P. Rateron, and C. W. Holyoke (2013), Hydrolytic weakening of olivine at mantle pressure: Evidence of [100](010) slip system softening from single-crystal deformation experiments, *Phys. Earth Planet. Inter.*, *216*, 12–20.
- Hart, S. R., E. H. Hauri, L. A. Oschmann, and J. A. Whitehead (1992), Mantle plumes and entrainment: Isotopic evidence, *Science*, *256*(5056), 517–520.
- Hernlund, J. W., P. J. Tackley, and D. J. Stevenson (2008), Buoyant melting instabilities beneath extending lithosphere: 1. Numerical models, *J. Geophys. Res.*, *113*, B04406, doi:10.1029/2006JB004863.
- Higgie, K., and A. Tommasi (2012), Feedbacks between deformation and melt distribution in the crust–mantle transition zone of the Oman ophiolite, *Earth Planet. Sci. Lett.*, *359–360*, 61–72.

- Higgie, K., and A. Tommasi (2014), Deformation in a partially molten mantle: Constraints from plagioclase lherzolites from Lanzo, western Alps, *Tectonophysics*, 615–616, 167–181.
- Hirth, G., and D. L. Kohlstedt (1996), Water in the oceanic upper mantle: Implications for rheology, melt extraction and the evolution of the lithosphere, *Earth Planet. Sci. Lett.*, 144, 93–108.
- Huang, J., S. Zhong, and J. van Hunen (2003), Controls on sublithospheric small-scale convection, *J. Geophys. Res.*, 108(B8), 2405, doi:10.1029/2003JB002456.
- Ishikawa, A., S. Maruyama, and T. Komiya (2004), Layered Lithospheric Mantle Beneath the Ontong Java Plateau: Implications from Xenoliths in Alnöite, Malaita, Solomon Islands, *J. Petrol.*, 45(10), 2011–2044.
- Jaupart, C., P. Molnar, and E. Cottrell (2007), Instability of a chemically dense layer heated from below and overlain by a deep less viscous fluid, *J. Fluid Mech.*, 572, 433–469.
- Jordan, T. H. (1979), Mineralogies, densities and seismic velocities of garnet lherzolites and their geophysical implications, in *The Mantle Sample: Inclusion in Kimberlites and Other Volcanics*, edited by F. R. Boyd and H. O. A. Meyer, pp. 1–14, AGU, Washington, D. C.
- Kaislaniemi, L., and J. van Hunen (2014), Dynamics of lithospheric thinning and mantle melting by edge-driven convection: Application to Moroccan Atlas mountains, *Geochem. Geophys. Geosyst.*, 15, 3175–3189, doi:10.1002/2014GC005414.
- Karato, S. I. (2010), Rheology of the Earth's mantle: A historical review, *Gondwana Res.*, 18(1), 17–45.
- Karato, S.-I., M. S. Paterson, and J. D. FitzGerald (1986), Rheology of synthetic olivine aggregates: Influence of grain size and water, *J. Geophys. Res.*, 91(B8), 8151–8176.
- Katz, R. F., M. Spiegelman, and C. H. Langmuir (2003), A new parameterization of hydrous mantle melting, *Geochem. Geophys. Geosyst.*, 4(9), 1073, doi:10.1029/2002GC000433.
- Korenaga, J., and T. H. Jordan (2002), On the state of sublithospheric upper mantle beneath a supercontinent, *Geophys. J. Int.*, 149(1), 179–189.
- Korenaga, J., and T. H. Jordan (2003), Physics of multiscale convection in Earth's mantle: Onset of sublithospheric convection, *J. Geophys. Res.*, 108(B7), 2333, doi:10.1029/2002JB001760.
- Le Roux, V., Bodinier, J.L., Tommasi, A., Alard, O., Dautria, J.M., Vauchez, and A. Riches (2007), The Lherz spinel-lherzolite: Refertilized rather than pristine mantle, *Earth Planet. Sci. Lett.*, 259, 599–612.
- Le Roux, V., A. Tommasi, and A. Vauchez (2008), Feedback between melt percolation and deformation in an exhumed lithosphere–asthenosphere boundary, *Earth Planet. Sci. Lett.*, 274(3–4), 401–413.
- Li, X., R. Kind, X. Yuan, I. Wolbern, and W. Hanka (2004), Rejuvenation of the lithosphere by the Hawaiian plume, *Nature*, 427(6977), 827–829.
- Lodge, A., and G. Helffrich (2006), Depleted swell root beneath the Cape Verde Islands, *Geology*, 34(6), 449–452.
- Mainprice, D., Tommasi, A., Couvy, H., Cordier, P. and Frost, D.J. (2005), Pressure sensitivity of olivine slip systems and seismic anisotropy of the Earth's upper mantle, *Nature*, 433, 731–733.
- Manglik, A., and U. R. Christensen (1997), Effect of mantle depletion buoyancy on plume flow and melting beneath a stationary plate, *J. Geophys. Res.*, 102(B3), 5019–5028.
- McKenzie D. (1985a), 230Th/238U disequilibrium and the melting processes beneath ridge axes, *Earth Planet. Sci. Lett.*, 72(2–3), 149–157.
- McKenzie, D. (1985b), The extraction of magma from the crust and mantle, *Earth Planet. Sci. Lett.*, 74(1), 81–91.
- McKenzie, D. (2000), Constraints on melt generation and transport from U-series activity ratios, *Chem. Geol.*, 162(2), 81–94.
- McKenzie, D., and M. J. Bickle (1988), The volume and composition of melt generated by extension of the lithosphere, *J. Petrol.*, 29(3), 625–679.
- Moore, W. B., G. Schubert, and P. Tackley (1998), Three-dimensional simulations of plume-lithosphere interaction at the Hawaiian swell, *Science*, 279(5353), 1008–1011.
- Morgan, W. J. (1972), Plate motions and deep mantle convection, *Geol. Soc. Am. Mem.*, 132, 7–22.
- Oxburgh, E. R., and E. M. Parmentier (1977), Compositional and density stratification in oceanic lithosphere-causes and consequences, *J. Geol. Soc. London*, 133(4), 343–355.
- Phipps Morgan, J., W. J. Morgan, and E. Price (1995), Hotspot melting generates both hotspot volcanism and a hotspot swell?, *J. Geophys. Res.*, 100(B5), 8045–8062.
- Ranalli, G. (2001), Mantle rheology: Radial and lateral viscosity variations inferred from microphysical creep laws, *J. Geodyn.*, 32(4), 425–444.
- Ribe, N. M. (2004), Earth science: Through thick and thin, *Nature*, 427(6977), 793–795.
- Ribe, N. M., and U. R. Christensen (1994), Three-dimensional modeling of plume-lithosphere interaction, *J. Geophys. Res.*, 99(B1), 669–682.
- Ribe, N. M., and U. Christensen (1999), The dynamical origin of Hawaiian volcanism, *Earth Planet. Sci. Lett.*, 171(4), 517–531.
- Richter, F. M. (1975), Convection and large-scale circulation of the mantle, *J. Geophys. Res.*, 78, 8735–8745.
- Riley, G. N., and D. L. Kohlstedt (1991), Kinetics of melt migration in upper mantle-type rocks, *Earth Planet. Sci. Lett.*, 105(4), 500–521.
- Ritzwoller, M. H., N. M. Shapiro, and S. J. Zhong (2004), Cooling history of the Pacific lithosphere, *Earth Planet. Sci. Lett.*, 226(1), 69–84.
- Rychert, C. A., G. Laske, N. Harmon, and P. M. Shearer (2013), Seismic imaging of melt in a displaced Hawaiian plume, *Nat. Geosci.*, 6(8), 657–660.
- Rychert, C. A., N. Harmon, and C. Ebinger (2014), Receiver function imaging of lithospheric structure and the onset of melting beneath the Galápagos Archipelago, *Earth Planet. Sci. Lett.*, 388, 156–165.
- Schmerr, N. (2012), The Gutenberg discontinuity: Melt at the lithosphere-asthenosphere boundary, *Science*, 335(6075), 1480–1483.
- Schubert, G., D. A. Yuen, and D. L. Turcotte (1975), Role of phase transitions in a dynamic mantle, *Geophys. J. R. Astron. Soc.*, 42(2), 705–735.
- Schutt, D. L., and C. E. Leshar (2006), Effects of melt depletion on the density and seismic velocity of garnet and spinel lherzolite, *J. Geophys. Res.*, 111, B05401, doi:10.1029/2003JB002950.
- Scott, D. R., and D. J. Stevenson (1989), A self-consistent model of melting, magma migration and buoyancy-driven circulation beneath mid-ocean ridges, *J. Geophys. Res.*, 94(B3), 2973–2988.
- Sleep, N. H. (1994), Lithospheric thinning by midplate mantle plumes and the thermal history of hot plume material ponded at sublithospheric depths, *J. Geophys. Res.*, 99(B5), 9327–9343.
- Sleep, N. H., and A. M. Jellinek (2008), Scaling relationships for chemical lid convection with applications to cratonic lithosphere, *Geochem. Geophys. Geosyst.*, 9, Q12025, doi:10.1029/2008GC002042.
- Soustelle, V., A. Tommasi, J. L. Bodinier, C. J. Garrido, and A. Vauchez (2009), Deformation and reactive melt transport in the mantle lithosphere above a large-scale partial melting domain: The Ronda Peridotite Massif, Southern Spain, *J. Petrol.*, 50(7), 1235–1266.
- Stüwe, K. (1995), Thermal buffering effects at the solidus. Implications for the equilibration of partially melted metamorphic rocks, *Tectonophysics*, 248(1–2), 39–51.
- Takei, Y., and B. K. Holtzman (2009a), Viscous constitutive relations of solid-liquid composites in terms of grain boundary contiguity: 1. Grain boundary diffusion control model, *J. Geophys. Res.*, 114, B06205, doi:10.1029/2008JB005850.
- Takei, Y., and B. K. Holtzman (2009b), Viscous constitutive relations of solid-liquid composites in terms of grain boundary contiguity: 2. Compositional model for small melt fractions, *J. Geophys. Res.*, 114, B06206, doi:10.1029/2008JB005851.

- Thoraval, C., A. Tommasi, and M.-P. Doin (2006), Plume-lithosphere interaction beneath a fast moving plate, *Geophys. Res. Lett.*, *33*, L01301, doi:10.1029/2005GL024047.
- Tommasi, A., and A. Ishikawa (2014), Microstructures, composition, and seismic properties of the Ontong Java Plateau mantle root, *Geochem. Geophys. Geosyst.*, *15*, 4547–4569, doi:10.1002/2014GC005452.
- Tommasi, A., M. Godard, G. Coromina, J.-M. Dautria, and H. Barszczus (2004), Seismic anisotropy and compositionally induced velocity anomalies in the lithosphere above mantle plumes: A petrological and microstructural study of mantle xenoliths from French Polynesia, *Earth Planet. Sci. Lett.*, *227*(3–4), 539–556.
- van Hunen, J., J. Huang, and S. Zhong (2003), The effect of shearing on the onset and vigor of small-scale convection in a Newtonian rheology, *Geophys. Res. Lett.*, *30*(19), 1991, doi:10.1029/2003GL018101.
- van Hunen, J., S. Zhong, N. M. Shapiro, and M. H. Ritzwoller (2005), New evidence for dislocation creep from 3-D geodynamic modeling of the Pacific upper mantle structure, *Earth Planet. Sci. Lett.*, *238*(1), 146–155.
- Villagomez, D. R., D. R. Toomey, D. J. Geist, E. E. E. Hooft, and S. C. Solomon (2014), Mantle flow and multistage melting beneath the Galapagos hotspot revealed by seismic imaging, *Nat. Geosci.*, *7*(2), 151–156.
- Walter, M. J. (1998), Melting of garnet peridotite and the origin of komatiite and depleted lithosphere, *J. Petrol.*, *39*(1), 29–60.
- Watson, S., and D. McKenzie (1990), Melt generation by plumes: A study of Hawaiian Volcanism, *J. Petrol.*, *32*(3), 501–537.